Electro-optic rotating half-waveplate for a quantum dot fine-structure eraser

by

Simon Daley

A thesis
presented to the University of Waterloo
in fulfillment of the
thesis requirement for the degree of
Master's of Applied Science
in
Electrical and Computer Engineering (Quantum Information)

Waterloo, Ontario, Canada, 2019

I hereby declare that I am the sole author of this thesis. This is a true copy of the thesis, including any required final revisions, as accepted by my examiners.

I understand that my thesis may be made electronically available to the public.

Abstract

Quantum dots are a promising source of entangled photon pairs. Recent advances have shown nearly dephasing-free entanglement from quantum dots embedded in semiconductor nanowires. An outstanding challenge with these sources is the presence of the so-called fine-structure splitting, which is the lifting of spin degeneracy of the exciton state due to quantum dot potential asymmetry. This fine-structure splitting causes the output state to precess rapidly, which is degrades the quality of measured entanglement due to finite detector temporal response and is undesirable for applications where preparation of a consistent state is needed. The effects of fine-structure splitting can be "erased" once the photons have been emitted using a flexible all-optical approach. This optical fine-structure eraser scheme requires a rapidly rotating half-waveplate, which cannot be implemented with commercially available off-the-shelf systems. This thesis presents the operation of an electro-optic modulator which can emulate a rotating half-waveplate at the required speeds, and demonstrates frequency conversion with an efficiency of 92%.

Acknowledgements

I would like to acknowledge those whose contributions are featured prominently in this thesis. The universal fine-structure eraser scheme was developed primarily by Andreas Fognini, with assistance from Arash Ahmadi and the rest of the authors of [1]. My primary contribution to that work was to propose how to implement the rotating half waveplate and pursue that avenue. The measurements of the quantum dot in Figure 3.2 and related work was done primarily by Andreas Fognini and Arash Ahmadi with assistance from the authors of [2]. The work in Chapter 5 was a joint effort with Michael Kobierski, with assistance from Andreas Fognini.

I would like to acknowledge those who supported the completion of this thesis. My supervisor Michael Reimer provided support and guidance when asked, and the space and trust I needed to do my work otherwise. Michael Kobierski was unfailingly generous with his time and knowledge, and I greatly benefited from his patience and honesty as we learned together. Morgan Mastrovich was always quick to offer help with practical tasks and conceptual understanding while sharing office and laboratory space. The other members of my research group provided essential support by offering their time and expertise and contributing the work necessary to operating and maintaining our laboratory. Harmeny Toope and Chris Dietrich provided the administrative support that allows us to focus on our research and kindly ensured that our workplace was always welcoming and orderly. Emma McKay and Nachiket Sherlekar provided feedback on a draft of this thesis.

I would like to thank those who supported me throughout this degree. In particular: my parents, grandparents and the rest of my family; Emma, Morgan, Carolyn, Al, Lindsay and the other FemPhys folks; Pamela, GRU, KAMM and the other members of my faith community. To those whose assistance I have forgotten or failed to mention, please accept my sincere apology and thanks.

Table of Contents

List of Figures

List of Tables

Abbreviations

DAC digital-to-analog converter 50, 52

EOM electro-optic modulator 1, 38, 41–44, 48, 50, 53–56, 58

FSS fine-structure splitting 1, 2, 8, 22–26, 28, 58

HWP half-waveplate 1, 26–28, 37, 45–47, 49, 50, 52, 58

LCP left circularly polarized 28, 53, 54

NPBS non-polarizing beamsplitter 47, 49

PBS polarizing beamsplitter 45, 52, 54

QWP quarter-waveplate 27, 46, 54

RCP right circularly polarized 28, 46, 53, 54

SPDC spontaneous parametric downconversion 2, 4, 5, 7, 8, 13, 58

List of Symbols

δ Fine-structure splitting, the difference in energy between the exciton's two ground spin states. 23, 24, 28, 46

ϕ Retardance, the optical path difference between light polarized parallel to the fast axis and light polarized parallel to the slow axis of a linear retarder. 26, 29, 31, 34

Chapter 1

Introduction and overview

Quantum dots are a promising source of entangled photons which have the potential to provide nearly on-demand operation. One of the primary outstanding challenges is fine-structure splitting (FSS), which results in rapid precession of emitted states. A proposal for erasing the state precession requires a rapidly rotating half-waveplate (HWP). This thesis presents a potential fast (hundreds of MHz to a few GHz) rotating HWP implementation capable of meeting the requirements of the FSS eraser.

Chapter 2 explains why quantum dots are worth pursuing as sources and provides information on the structure and operation of the nanowire-embedded quantum dot source the rotating HWP was designed to be used with. Chapter 3 provides background on the origins and effects of FSS, as well as how to erase it. Chapter 4 introduces the particular type of electro-optic modulator (EOM) which can be used to emulate a rotating HWP. Chapter 5 describes measurements made to demonstrate the desired operation of the EOM.

Chapter 2

Nanowire-embedded quantum dots as sources of entangled photon pairs

The purpose of this chapter is to show why erasing FSS in a quantum dot is a useful goal. I will discuss uses and requirements of entangled photons, explain why quantum dots present an attractive alternative to spontaneous parametric downconversion (SPDC) sources, and provide a brief overview and performance comparison of various nanostructures for extracting photons from quantum dots.

2.1 Uses and requirements for entangled photon pairs

Entanglement was first postulated in 1935 as the Einstein, Podolsky and Rosen (EPR) paradox [3]. Though it was intended to suggest that quantum mechanics was an incomplete theory because it violated local realism, Bell [4] and later Clauser, Horne, Shimony and Holt [5] proposed experiments that use it as a way to disprove the so-called hidden variable theories proposed as an alternative.

Though early interest in entanglement was focused on fundamental quantum optics experiments, there has been considerable interest over recent decades in applications that

make use of entanglement and other quantum mechanical effects for metrology [6], sensing [7], increasing the density [8] and security [9] of communication, and performing classically impracticable computing tasks such as factoring large numbers [10] and simulating quantum systems [11, 12].

The polarization state of photons has been a favoured physical system for demonstrating and making use of entanglement since the earliest experiments, particularly for quantum communication schemes where photons' vanishingly small nonlinear interaction in most media is a desirable quality. The control of polarization states of light has been well understood for over a century, and the increasing ubiquity of commercial fibre-optic communication technologies has led to a variety of robust, low-cost options for generating, controlling and detecting polarized light.

2.1.1 Requirements

The main requirements of a source of entangled photon pairs are high entanglement fidelity, indistinguishability, extraction efficiency and low multi-pair emission [13]. Additional desirable features include the possibility for integration on photonic chips and with existing telecommunication infrastructure, low cost and ease of fabrication and operation, and scalability.

In a source with high indistinguishability, photon pairs generated at different times are quantum mechanically identical. Low multi-pair emission means that for each trigger, no more than one pair of entangled photons is emitted. Extraction efficiency refers to the probability that a photon is generated and collected by optics. Fidelity is a measure of how similar two quantum systems are, and entanglement fidelity is a way of quantifying how entangled a system is by describing its fidelity to the closest maximally entangled state.

2.2 Sources of entangled photon pairs

There are a number of physical systems which can be used to generate entangled photon pairs. The first source to violate Bell's inequality used an atomic cascade in sodium atoms [14], though this method was abandoned in favour of semiconductor devices due to the technical advantages, which include the relative ease and low cost of fabrication and use, as well as the greater potential for scalability and compatibility with integrated optics. Orieux *et al.*'s review article provides an overview of these devices and recent developments in the field [15].

An alternative to directly generating entanglement was proposed in Knill, Laflamme and Millburn's 2001 proposal for linear optical quantum computing (LOQC) [16], which opened the possibility of generating entanglement using only a single photon source, linear optics, and photodetectors. The process relies on the interference of two indistinguishable photons at a beamsplitter to generate path entanglement through the Hong-Ou-Mandel effect [17]. A controlled-not (CNOT) gate, which generates entanglement and is a basic element of LOQC [18], was experimentally realized using integrated optics shortly thereafter [19]. The success of a linear optical CNOT gate can be at most 75% [20]. Though this doesn't degrade the quality of entanglement because it is possible to identify and discard photons from unsuccessful attempts, it does make deterministic operation impossible.

In the following section, I'll discuss the fundamental performance limitation of SPDC, its current state-of-the-art, and discus why quantum dots have the potential to outperform SPDC if current technical challenges are overcome.

2.2.1 Spontaneous parametric downconversion

SPDC sources have been considered the best source of high quality polarization-entangled photon pairs since Kwiat *et al.*'s 1995 violation of Bell's inequality using an SPDC source [21]. More recently, they were used in all three loophole-free tests of Bell's theorem independently published in 2015 [22, 23, 24]. Entanglement is generated in SPDC sources

by sending photons with frequency ω_0 an momentum k_0 into a non-linear optical crystal, which has some probability of interacting with each photon to produce two photons with frequencies $\omega_1 + \omega_2 = \omega_0$ and momenta $k_1 + k_2 = k_0$. Due to dispersion and birefringence in the crystal, the photons must meet specific phase-matching conditions, giving predictable polarizations and directions of emission. SPDC sources are relatively inexpensive and can be operated at room temperature, though the need for optical pumping (which is expensive and bulky) limits their commercial potential.

Though the quality of SPDC sources continues to improve as technical challenges are overcome, their brightness is fundamentally limited by their statistical nature [25]. As the intensity of the pulsed or continuous wave (CW) excitation is increased, so does the probability of emitting multiple pairs of entangled photons. The fidelity of the entangled state is degraded, because there is a chance that the two photons chosen will be from different pairs, which would have no quantum correlations. Efforts to achieve higher count rates without degrading fidelity require considerable sophistication and complexity, and have included temporal multiplexing by using smaller pulses with a higher repetition rate [26] and other multiplexing techniques, as well as using non-linear effects to create a blockade [27].

Fidelity of Poissonian sources

We can find the fidelity over multiple measurements by considering an ensemble state [28] where one photon is chosen from both the idler and signal modes for each pulse that generates at least one pair. We'll ignore any imperfections in the collection and detection of the photons to get the "best case scenario". The probability that a pulse will generate n pairs of photons is given by the Poisson distribution [29]

$$P(n) = e^{-\mu}\frac{\mu^n}{n!} \tag{2.1}$$

where μ is the probability of generating a pair of photons with a single pulse, and $e^{-\mu}$ is a normalization constant so that the total probability over every possible number of photon pairs is unity.

Our pair source efficiency, which we'll define as the probability of generating at least one pair of photons, rather than the probability of generating a single pair (these two definitions are equivalent for sources which display perfect antibunching, meaning there is zero chance of multiple photons being emitted at the same time), is

$$B = 1 - P(0) = 1 - e^{-\mu} \tag{2.2}$$

If each pair of photons has perfect fidelity to a known maximally entangled pure state $\rho_0 = |\Psi\rangle\langle\Psi|$, our measured density operator, considering only pulses where $n \geq 1$ pairs of photons have been generated is

$$\rho = \frac{1}{1 - P(0)} \sum_{n=1}^{\infty} P(n) \left(P_s(n)\rho_0 + P_d(n)\rho_d \right) \tag{2.3}$$

where $P_s(n) = \frac{1}{n}$ is the probability the two measured photons are from the same pair, $P_d(n) = \frac{n-1}{n} = 1 - \frac{1}{n}$ is the probability that they are from different pairs, and $\rho_d = \mathrm{Tr}_i[\rho_0] \otimes \mathrm{Tr}_s[\rho_0]$ describes the case where the measured photons are from different pairs [30]. The fidelity to ρ_0 is [15]

$$F = \mathrm{Tr}[\rho\rho_0] = \frac{1}{1 - P(0)} \sum_{n=1}^{\infty} P(n) \left(P_s(n) + \frac{1}{2} P_d(n) \right) \tag{2.4}$$

Figure 2.1 shows the relationship between equations 2.4 and 2.2. Because we only measure cases where at least one pair of photons is emitted, the fidelity approaches 1, the value we would expect for a maximally entangled state, as the pair source efficiency approaches zero. It approaches 0.5, the value we would expect for a state with zero entanglement, as the pair source efficiency approaches 100%.

2.2.2 Quantum Dots

Quantum dots are semiconductor structures typically consisting of a few thousand atoms surrounded by a higher bandgap material in all three dimensions. The high degree of

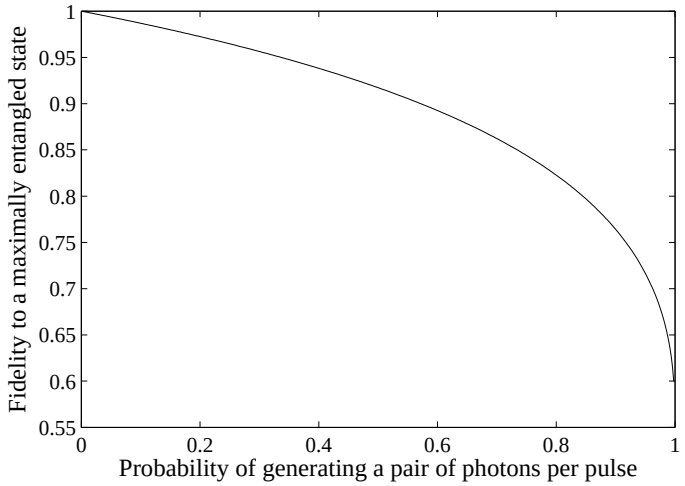

Figure 2.1: Plot of fidelity to a maximally entangled state (F) versus probability of generating a pair of photons per pulse (B) for SPDC sources.

confinement leads to a density of state function consisting of discrete levels. In a symmetric quantum dot, these levels produce optical spectra similar to orbitals in atoms, and for this reason quantum dots are often referred to as "artificial atoms".

Benson *et al.* proposed in 2000 that a quantum dot could be used to generate entanglement through a similar process to an atomic cascade [31]. This so-called "exciton-biexciton cascade" is the process most commonly used to generate entangled photons using quantum dots, and is explained in greater detail in Section 3.1.

A "biexciton" refers to the state of a quantum dot when there are two electrons and two holes occupying its ground state. Due to the Pauli exclusion principle, there can be only one spin up and one spin down each of both the electrons and holes in the ground state. This leads to antibunching if the time it takes for the quantum dot to relax back to the ground state is much longer than the optical or electrical pulse that populates it. This allows for deterministic operation, as we can populate the quantum dot with a very high probability without risking multi-pair emission. Due to binding energy, the biexciton has a lower energy than twice that of an exciton, which means that photons emitted from the

two steps of recombination will have slightly different wavelengths and can be separated.

Performance barriers

Despite their promise, quantum dots continue to be outperformed by SPDC for most applications due to the lower quality of entanglement and low collection efficiencies. One of the primary ways fidelity is degraded in quantum dots is through dephasing. This can be caused by a variety of mechanisms, including quantum dot asymmetry and the electromagnetic environment around the dot due to stray magnetic fields, electric fields, or charged particles.

Measured entanglement can be lower than actual entanglement due to imperfections in detection, such as long integration times over a rapidly evolving state [2]. The evolution of the state is caused by FSS, which is discussed in Section 3.2.

2.2.3 Nanostructures for extracting photons

A photon is only useful if it can be collected. While quantum dot sources can generate photon pairs with very high efficiency, difficulties collecting and directing the emitted photons into an optical system so that they can be used reduce the brightness considerably. For this reason, they are typically embedded in nanostructures. A review of recent developments in the field of quantum dot polarization-entangled photon sources with a comparison of nanostructures was published by Huber *et al.* in 2018 [32].

Extraction efficiency in bare quantum dots

Bare quantum dots typically have extraction efficiencies of less than 2% due to two factors: total internal reflection and omnidirectional emission [33]. Consider a quantum dot on a substrate with index of refraction n surrounded by free-space or some material with a refractive index close to 1 (see Figure 2.2). To achieve the symmetric 3D confinement needed,

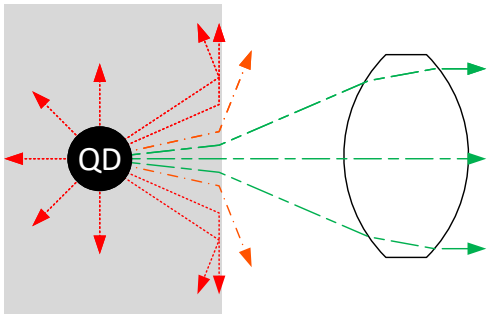

Figure 2.2: Factors affecting extraction efficiency of a bare quantum dot (black) embedded in a substrate (grey). More than 97% of the photons do not exit the substrate (red dotted lines), either because they are emitted in the wrong direction, or because they are reflected back into the substrate at the interface. A substantial portion of the photons which exit the substrate are emitted outside of the acceptance angle of the first lens (orange dot-dash lines). Only photons which both exit the device and enter the first lens are extracted and directed into the optical system for further use (green dashed lines).

the lower bandgap quantum dot region needs to be completely surrounded by the higher bandgap substrate material. Assuming the quantum dot is approximately symmetric, photons will be emitted in all directions with roughly equal probability. Using the critical angle of incidence for total internal reflection at the substrate edge $\theta_c = \arcsin(n^{-1})$, we can compute the fraction of photons that would be emitted within a cone with half angle θ_c (and would be able to exit the device)

$$\frac{\int_0^{\theta_c} \sin(\phi) d\phi}{\int_0^{\pi} \sin(\phi) d\phi} = \frac{1}{2}(1 - \cos\theta_c) = \frac{1}{2}\left(1 - \sqrt{1 - \frac{1}{n^2}}\right) \tag{2.5}$$

For an InP substrate, which has a refractive index of about 3.4, the critical angle of incidence for total internal reflection is approximately $\theta_c = 17.1^o$ and the fraction of light that can exit the device is about 2.2%. For GaAs ($n \approx 3.5$), the critical angle is $\theta_c = 16.6^o$ and the fraction of light that exits the device is about 2.1%.

Collection efficiency further limits our extraction efficiency, as collection optics have a finite acceptance angle. This would limit our extraction efficiency to 50% even if the photons weren't reflected or refracted at the substrate-air interface and the first lens had acceptance angle of 90^o. The numerical aperture of lenses and objectives are typically much lower. Coupling to waveguides requires further consideration of the mode profile in addition to acceptance angle which leads to greater losses.

As we've seen, our extraction efficiency can be improved by increasing the directionality of the quantum dot's emission so that more photons make it to the surface of the surrounding material, increasing the portion of photons which are aren't reflected back into the substrate at the surface, and improving the directionality and mode profile of the emission from the surface of the substrate so that the photons can be collected by a lens or waveguide.

Types of nanostructures

Extraction efficiency for quantum dot nanostrucutres is generally thought of as a product of the coupling efficiency (or the portion of emitted photons which are coupled to the desired mode of the nanostructure) and the collection efficiency (or the portion of photons from the desired mode which can be collected by a lens once emitted). Nanostructures for improving quantum dot extraction efficiency can be categorized by which of these factors they target for improvement. Geometric approaches focus on reducing total internal reflection and increasing directionality of emitted photons (lens). Micropillars increase emission into a desired mode though Purcell enhancement (cavity), while nanowires suppress emission into undesirable modes (waveguide).

Geometric approach The geometric approach creates a structure immediately above the quantum dot that reduces total internal reflection and reduces the emission angle of the light. It doesn't effect the quantum dot itself, but rather acts on the photons through reflection and refraction once they have been emitted. A reflective structure can be added below the quantum dot to redirect photons emitted in the wrong direction. A recent example is Chen *et al.*'s "photonic antenna" which has a fidelity of $(90 \pm 3)\%$ and a pair source efficiency of $(37.2 \pm 0.2)\%$ [34].

Cavity approach The operating principle of these is the Purcell effect, which accelerates spontaneous emission into a desired mode in the weak coupling regime of a cavity [29]. This is typically achieved by embedding a layer of self-assembled quantum dots between two distributed Bragg reflector (DBR) mirrors, with the top one being slightly less reflective, then etching a micropillar around a quantum dot identified as having desirable optical properties in photoluminescence measurements. The fabrication process is extremely technically challenging and typically not deterministic, though improvements continue to be made [35].

The cavity approach is generally preferred for single quantum dot photon sources, as in addition to increasing extraction efficiency they improve the indistinguishability of

photons emitted by subsequent pulses [36]. The microcavity approach is difficult to apply to entangled photon sources, because the narrow wavelength bandwidth of the cavities precludes efficient coupling of both the exciton and biexciton photons which usually have different wavelengths due to the biexciton binding energy. In 2010 Dousse *et al.* [37] realized a bright quantum dot source with a pair emission probability per pulse of 12% and entanglement fidelity of 67% using a double-micropillar structure. The two pillars' separation was tuned to produce two different narrowband cavity modes which the exciton and biexciton could couple to. Although attractive, realization of the double-micropillar structure is technically complex and a repeat demonstration has not been made.

A recent variation of this is Wang *et al.*'s [38] circular Bragg grating bull's-eye cavity, which offers broad-band coupling. Their source combines high fidelity and pair efficiency (36.7% and 90%, respectively), values almost identical to Chen *et al.*

Waveguide approach Instead of stimulating spontaneous emission into a desired mode, waveguide structures suppress spontaneous emission into all other modes. This allows for good coupling over a wide range of photon energies, removing the difficulty of coupling to both the exciton and biexciton photons.

Tapered nanowires with a quantum dot embedded on-axis can be grown deterministically, and have robust insensitivity to small variations in fabrication parameters. The fabrication process involves placing gold particles on a substrate at regular intervals, under which narrow columns of the substrate material will start vapour-liquid-solid growth. The quantum dots are integrated by briefly introducing an additional element into to the growth reactor. After further axial growth, the width of the nanowires is increased to encase the quantum dot radially by raising the temperature to favour radial growth and suppress axial growth. A narrow taper at the tip, which reduces reflection by allowing the coupled mode to leak adiabatically, can be produced by not completely suppressing axial growth. The nanowires can be transferred onto a broadband mirror (typically gold), though precise positioning is crucial to avoid destructive interference. Our most recently published results for this type of device give a fidelity of 88% at a pair source efficiency of 1.6% [2].

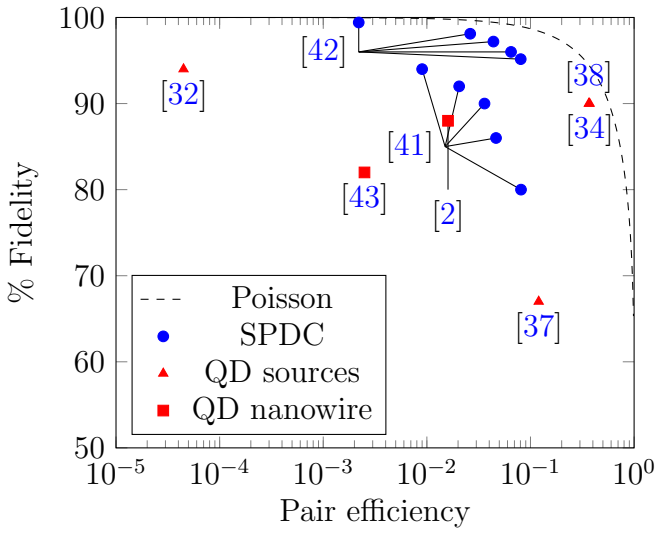

Figure 2.3: Comparison of the performance of entangled photon sources consisting of quantum dots embedded in different nanostructures described in the previous section to the theoretical upper limit and actual performance of SPDC sources. Adapted and modified from [43] with assistance from the author.

2.2.4 Performance comparison

Figure 2.3 plots the entanglement fidelity and pair source efficiency for the sources discussed above. In addition to currently producing lower fidelity pairs, most quantum dot sources still require cryogenic cooling (generally to 4K) to minimize dephasing, making them expensive and difficult to transport relative to SPDC sources. Like SPDC sources, they are mostly still optically pumped, further limiting portability. There is, however, nothing in principle prohibiting the development of quantum dot sources that have a better combination of brightness and entanglement fidelity than is achievable with SPDC, are electrically-pumped [39], and can be operated at higher temperatures [40].

2.3 Device particulars

A detailed account of how the quantum dot whose fine-structure this experiment set out to erase was grown at the National Research Council of Canada is beyond the scope of this thesis, as I was not involved in the sample's fabrication or characterization. The interested reader is directed to [44, 45] for fabrication details.

The nanowires are grown using a selective-area (SA) vapor–liquid–solid (VLS) process, represented schematically in Figure 2.4. 20nm gold particles, which are deposited in a grid pattern at the centre of holes in an SiO_2 mask on the InP wafer, catalyse growth of the nanowire core. The quantum dot is grown at this stage by briefly introducing As into the growth chamber, resulting in an few-nanometres ($\sim$ 6nm) thick InAsP section in the InP nanowire core. Once the core has reached the desired height, the growth conditions are changed to allow deposition along the bare InP of the nanowire and wafer (in the holes in the SiO_2 mask). The precise growth conditions determine how much upwards versus outwards growth is favoured during this stage, giving the smooth taper the nanowire tip.

2.3.1 Structure and properties

Electronic properties of bulk InP and InAsP

Electrons in the lowest energy conduction band in wurtzite InP and InAsP occupy an s-like orbital with band angular momentum $L = 0$, which with the electron spin $S = 1/2$ gives total angular momentum $J = 1/2$ with a projection along the z-axis $j_z = \pm 1/2$. Holes at the top of the valence band occupy one of 3 p-like ($L = 1$) orbitals, which in wurtzite are non-degenerate due to anisotropy between the c-axis ([001] direction, along the axis of the nanowire), the the plane perpendicular to it ((001) plane, along the nanowire's radial direction) (crystal field splitting), and spin-orbit coupling.

The lowest of the three p-like sub-bands is a few hundred meV below the top of the valence band (145.0meV in InP and 352.7meV in InAs [46]), and can be disregarded. The

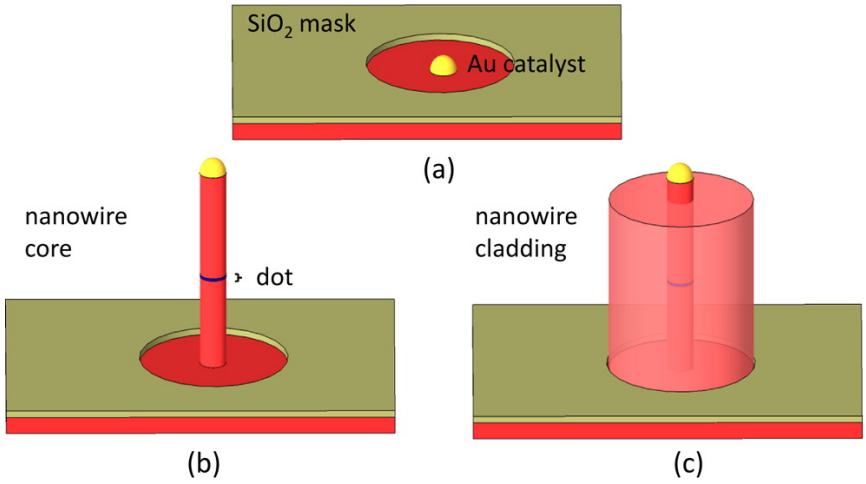

Figure 2.4: Schematic illustration of the SA-VLS growth process: (a) The nanowires are grown on a patterned substrate consisting of circular openings in a SiO_2 mask in which gold catalysts are deposited by a self-aligned lift-off process. (b) The nanowire core is grown using growth conditions that promote catalyzed growth while minimizing substrate growth. (c) Conversely, the nanowire cladding is grown by minimizing catalyzed growth while promoting substrate growth. Reprinted with permission from [44]. Copyright 2012 American Chemical Society.

energy separation between the top two sub-bands (typically labelled heavy and light holes) is 59.2meV in InP and 35.4meV in InAs [46]. This separation is increased with tight confinement and there is typically minimal intersub-band mixing observed in quantum dots [47], so we will consider only heavy holes, which have $J = 3/2$, $j_z = \pm 3/2$.

Bandgap and effective mass values are shown in Table 2.1. Note that there are different values depending on whether we are parallel to the crystal's c-axis (axial direction), or perpendicular to it (radial direction).

The quantum dot can be approximated by a cylindrical or "hockey puck" shape with a diameter of $25 - 30$nm and a height of ~ 6nm [45, 47]. The confining potential can be written as a product of the axial and radial components $V(x, y, z) = V(z)V(r)$. We'll now consider each component separately.

	InP	InAs	$InAs_{0.25}P_{0.75}$
Bandgap E_g [eV]	1.494	0.467	1.237
Axial electron effective mass $m^*_{e_\parallel}/m_0$	0.0947	0.0370	0.0803
Axial heavy hole effective mass $m^*_{hh_\parallel}/m_0$	1.0646	0.9738	1.0419
Radial electron effective mass $m^*_{e_\perp}/m_0$	0.1183	0.0416	0.0991
Radial heavy hole effective mass $m^*_{hh_\perp}/m_0$	0.1988	0.1046	0.1753

Table 2.1: Bandgap and effective masses in wurtzite InP and InAs [46]. Values for $InAs_{0.25}P_{0.75}$ were obtained by linear interpolation between the values for InP and InAs.

Axial confinement

The axial potential is well approximated by a finite square well (see Figure 2.5). The confinement energies are found by numerically solving the following transcendental equations, which arise from application of even or odd boundary conditions

$$k_{InP} = \begin{cases} k_{InAsP} \tan\left(k_{InAsP}\frac{L}{2}\right), & \text{Even} \\ -k_{InAsP} \cot\left(k_{InAsP}\frac{L}{2}\right), & \text{Odd} \end{cases} \tag{2.6}$$

where $k_{InP} = \sqrt{2m_{InP}(E+\Delta E)}/\hbar$ and $k_{InAsP} = \sqrt{2m_{InAsP}\Delta E}/\hbar$, and $m_{InP,InAsP}$ are the effective masses along the axial direction in InP and InAsP from Table 2.1. The ground state confinement energy is the lowest energy even solution, and the first excited state confinement is the lowest energy odd solution. The confinement energy as a function of quantum dot height computed using the values in Table 2.1 is shown in Figure 2.5.

Note that for a typical quantum dot ($L < 6$nm) only the ground state is available for both electrons and holes, and the separation between the ground state and first excited state is much larger than the separation between states in the radial direction (see Figure 2.6). This means that the energy level structure near the ground state is determined by the radial confinement.

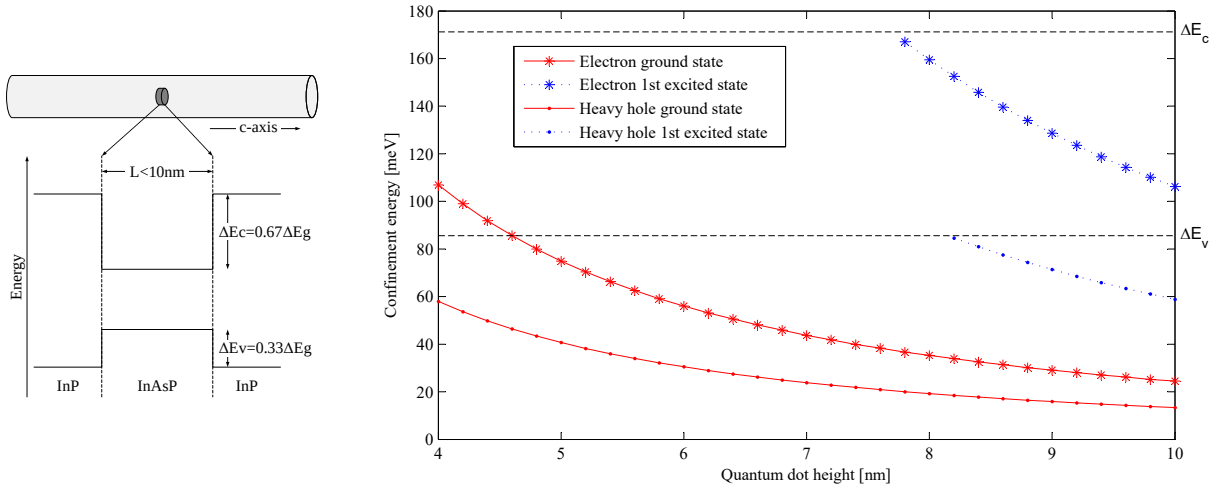

Figure 2.5: Axial confinement of electrons and holes. The left figure shows a schematic representation of the quantum dot embedded in the nanowire above a energy level diagram for the region of interest. The right plot shows numerical solutions to Equation 2.6 for the electron ground state ($E_0^e(L)$) and first excited state, and the heavy hole ground state ($E_0^{hh}(L)$) and first excited state.

Radial confinement

The potential in the radial plane is a finite circular well. The bound solutions are of the form [48]

$$\psi_m(r,\phi) \propto \begin{cases} J_{|m|}(k_{InAsP}r)e^{(im\phi)}, & r \leq R \\ K_{|m|}(k_{InP}r)e^{(im\phi)}, & r > R \end{cases} \tag{2.7}$$

where J_m is a Bessel function of the first kind, K_m is a modified Bessel function of the second kind, r is the radial distance from the centre of the quantum dot, and ϕ is an angle providing the second parameter needed to describe the position within the radial plane. A transcendental equation for energy can be found by imposing continuity at the boundary, and taking the ratio of the function and its first derivative to eliminate the normalization factor

$$k_{InAsP}\frac{J'_{|m|}(k_{InAsP}r)}{J_{|m|}(k_{InAsP}r)} = k_{InP}\frac{K'_{|m|}(k_{InP}r)}{K_{|m|}(k_{InP}r)} \tag{2.8}$$

Numerical solutions, along with solutions evenly spaced above the ground state (as would be expected with a harmonic oscillator) are shown in Figure 2.6. The solutions are similar to those for a isotropic harmonic oscillator, and experimental observations have validated this approximation for self-assembled quantum dots [47].

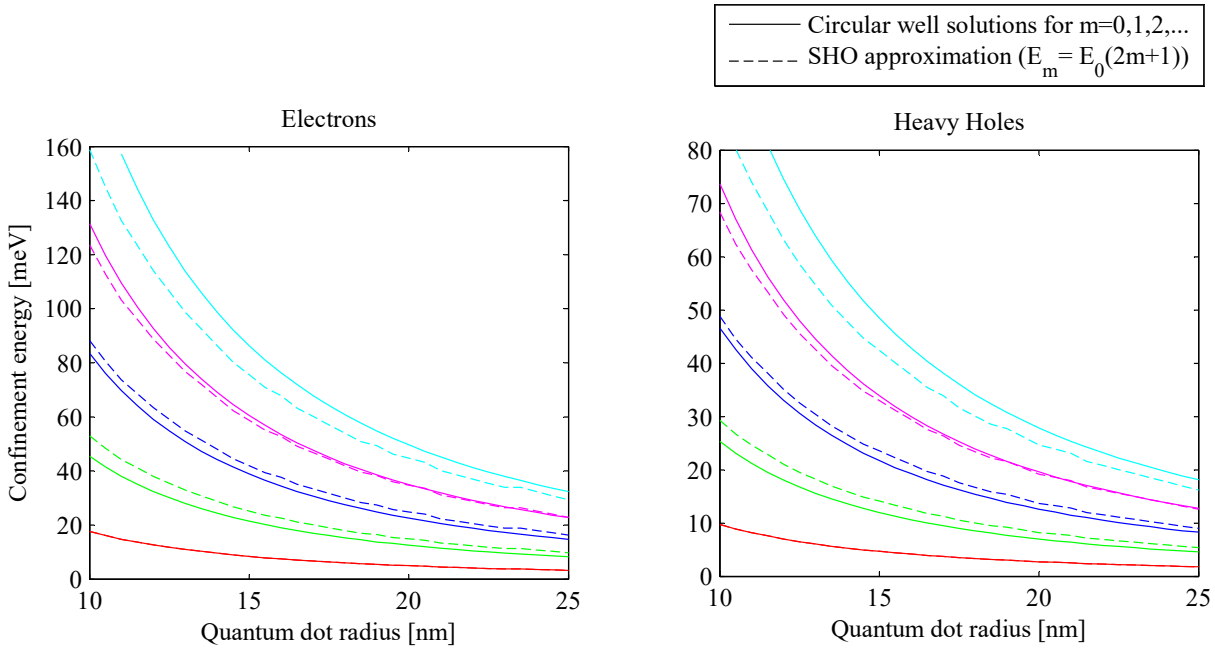

Figure 2.6: Radial confinement of electrons and holes. Solid lines are numerical solutions to Equation 2.8 for the electrons ($E^e_{0,1,2,3,4}(R)$, left) and heavy holes ($E^{hh}_{0,1,2,3,4}(R)$, right). Dashed lines are evenly spaced solutions above the ground state $E^{e,hh}_0(R)$.

Figure 2.7 shows the energy of the exciton ground state ($E_0 = E_g + E_0(L) + E_0(R)$) as a function of the quantum dot height and radius using values for $E_0(L) = E^e_0(L) + E^{hh}_0(L)$

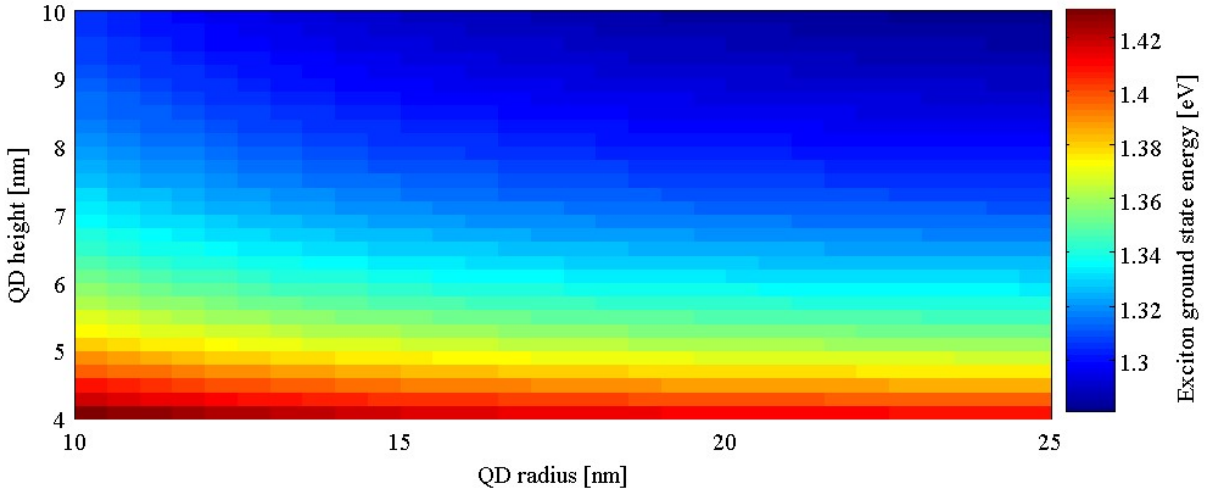

Figure 2.7: Numerical solutions for exciton ground state energy as a function of quantum dot dimensions.

and $E_0(R) = E_0^e(R) + E_0^{hh}(R)$ from Figures 2.5 and 2.6, and E_g for $In_{0.75}As_{0.25}P$ from Table 2.1.

Solutions to the 2-dimensional isotropic harmonic oscillator have energies

$$E = \hbar\omega(n_x + n_y + 1) \tag{2.9}$$

where $n_{x,y} = 0, 1, 2, \ldots$. Defining $n = n_x + n_y$, we have energy levels $E_n = \hbar\omega(n+1)$ with degeneracies of $g_n = \binom{1+n}{n} = n + 1 = 1, 2, 3, \ldots$. The energy levels are commonly labelled following the convention for atomic orbitals as 's', 'p', 'd', etc. Each energy level can be occupied by two electrons/holes of opposite spin (Pauli exclusion principle).

When excited non-resonantly, a brief, high-intensity, above-bandgap pulse produces electrons and holes, some of which fall into the quantum dot and will tend to relax to lower energy states through phonon interactions. The pulse intensity is set high enough to ensure that enough electrons and holes are generated that the lowest energy level becomes occupied with near certainty (See Figure 2.8). A detailed description of excitation schemes

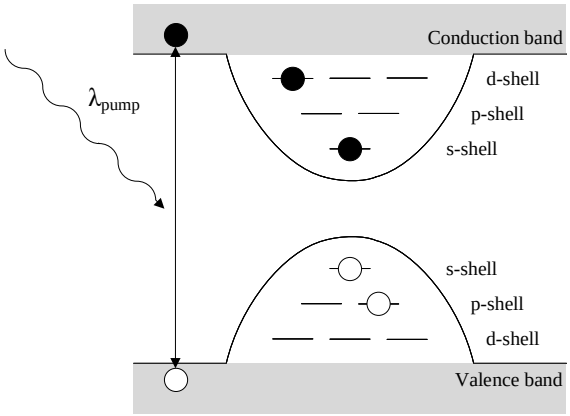

Figure 2.8: Non-resonant excitation of quantum dot showing a schematic representation of the harmonic radial confinement potential with the density of states of the solutions.

and performances can be found in [49]. For our purposes, we will consider recombination starting with a biexciton in its ground state without specifying how that came to be.

Chapter 3

Quantum dot fine-structure splitting

3.1 Biexciton-exciton cascade

3.1.1 Optical selection rules

As discussed in the previous section, the quantum dot's ground state is occupied by heavy holes with $j_z = \pm 3/2$ and electrons with $j_z = \pm 1/2$ and the biexciton will include one spin up and one spin down each of both the electrons ($|\uparrow\downarrow\rangle$) and holes ($|\Uparrow\Downarrow\rangle$). A photon emitted via recombination has to have the same angular momentum as the electron and hole, so the optically allowed combinations of electron and heavy hole recombinations are $|\uparrow\Downarrow\rangle$ and $|\downarrow\Uparrow\rangle$, which have net angular momenta of -1 and $+1$ producing photons that are left and right circularly polarized, respectively.

3.1.2 Polarization state

There are two possible recombination paths (see Figure 3.1), one each for the two possible exciton states $|X_L\rangle = |\uparrow\Downarrow\rangle$ and $|X_R\rangle = |\downarrow\Uparrow\rangle$. In the absence of which-path information,

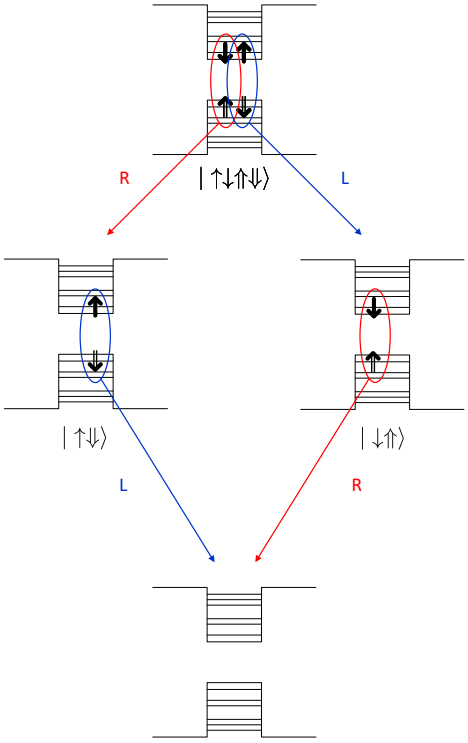

Figure 3.1: The two possible radiative recombination paths for a biexciton in a quantum dot with zero FSS. Red arrows represent the emission of a right circularly polarized photon, and blue arrows a left circularly polarized photon.

the two decay paths $|\uparrow\Downarrow\downarrow\Uparrow\rangle \rightarrow |L_{XX}, X_R\rangle \rightarrow |L_{XX}, R_X\rangle$ and $|\uparrow\Downarrow\downarrow\Uparrow\rangle \rightarrow |R_{XX}, X_L\rangle \rightarrow |R_{XX}, L_X\rangle$ combine to form the entangled final two-photon state $\Psi = \frac{1}{\sqrt{2}}(|LR\rangle + |RL\rangle)$. We can rewrite this in the HV basis using $|R\rangle = \frac{1}{\sqrt{2}}(|H\rangle + i|V\rangle)$ and $|L\rangle = \frac{1}{\sqrt{2}}(|H\rangle - i|V\rangle)$: $|\Psi\rangle = \frac{1}{\sqrt{2}}(|HH\rangle + |VV\rangle)$, which is a Bell state.

3.2 Fine-structure splitting cause and results

FSS is a difference in energy between the two possible exciton states $|X_L\rangle = |\uparrow\Downarrow\rangle$ and $|X_R\rangle = |\downarrow\Uparrow\rangle$. The FSS energy δ is proportional to [50]

$$\delta = 2K\beta\xi(1-\xi)\frac{1}{(l_y^{eh})^3} \tag{3.1}$$

where K is a constant that depends on the quantum dot material properties, $\beta = |\langle\Psi_e|\Psi_h\rangle|^2$ is proportional to the overlap between the electron and hole wavefunctions, l_y^{eh} is the length along y of the exciton's electron and hole hybrid wavefunction, and $\xi = (l_y^{eh}/l_x^{eh})$ is related to the eccentricity of the exciton wavefunction. Asymmetry in the confining potential causes a non-zero value of $(1-\xi)$, which occurs when the solutions in the xy plane are no longer well approximated by the isotropic parabolic potential used in Section 2.3.1, but is instead closer to an asymmetric parabolic potential. Strain and quantum dot composition also contribute to the FSS.

3.2.1 Time evolution of polarization state

When the fine structure splitting is non-zero the exciton eigenstates, symmetric $|X_H\rangle = \frac{1}{\sqrt{2}}(|X_R\rangle + |X_L\rangle)$ and antisymmetric $|X_V\rangle = \frac{-i}{\sqrt{2}}(|X_R\rangle - |X_L\rangle)$ superpositions of the spin-up and spin-down exciton states, are separated by FSS energy δ [51].

The spin-up or spin-down exciton state left by the emission of the biexciton photon is a superposition of the eigenstates of the exchange interaction Hamiltonian (see [51] for Hamiltonian with derivation). The Hamiltonian does not depend on time, so we can write the solution to the time dependent Schrödinger equation as a superposition of its eigenstates, with the probability amplitudes determined by the initial preparation.

Our two recombinations paths for biexciton to exciton from the degenerate case can be rewritten in the eigenbasis: $|XX_L, X_R\rangle \rightarrow \frac{1}{\sqrt{2}}(|H_{XX}\rangle - i|V_{XX}\rangle)(|X_H\rangle + i|X_V\rangle)$ and

$|XX_R, X_L\rangle \rightarrow \frac{1}{\sqrt{2}}(|H_{XX}\rangle + i|V_{XX}\rangle)(|X_H\rangle - i|X_V\rangle)$. In the absence of which path information where we have an equal superposition of the two paths, the total state can be written: $\frac{1}{\sqrt{2}}(|L_{XX}, X_R\rangle + |R_{XX}, X_L\rangle) = \frac{1}{\sqrt{2}}(|H_{XX}, X_H\rangle + |V_{XX}, X_V\rangle)$. The exciton state evolves with time due to the non-degeneracy, precessing with frequency $\delta/\hbar$. The biexciton photon remains entangled to the exciton spin state to conserve angular momentum, so the states will evolve with time together:

$$|Ph_{XX}, X_{QD}\rangle = \sum_n a_n e^{iE_n t/\hbar}|\psi_n\rangle \tag{3.2}$$

$$= \frac{1}{\sqrt{2}}e^{i(E_o+\delta/2)t/\hbar}|H_{XX}, X_H\rangle + \frac{1}{\sqrt{2}}e^{i(E_o-\delta/2)t/\hbar}|V_{XX}, X_V\rangle \tag{3.3}$$

$$= \frac{1}{\sqrt{2}}e^{i(E_o+\delta/2)t/\hbar}\left(|H_{XX}, X_H\rangle + e^{-i\delta t/\hbar}|V_{XX}, X_V\rangle\right) \tag{3.4}$$

The final two-photon state after the exciton recombines after time $\tau = t_X - t_{XX}$ (t_X is the time of the exciton t_{XX} is the time of the biexiton emission), neglecting global phase, is

$$|\Psi\rangle = \frac{1}{\sqrt{2}}\left(|HH\rangle + e^{-i\delta\tau/\hbar}|VV\rangle\right) \tag{3.5}$$

The difference in concurrence between the Bell states $|\Phi^+\rangle = \frac{1}{\sqrt{2}}(|HH\rangle + |VV\rangle)$ and $|\Phi^-\rangle = \frac{1}{\sqrt{2}}(|HH\rangle - |VV\rangle)$ oscillates:

$$\langle\Phi^+|\Psi\rangle - \langle\Phi^-|\Psi\rangle = \frac{1}{2}(1 + e^{-i\delta\tau/\hbar}) - \frac{1}{2}(1 - e^{-i\delta\tau/\hbar}) \tag{3.6}$$

$$= e^{-i\delta\tau/\hbar} \tag{3.7}$$

This has been observed experimentally (see figure 3.2), which validates the proposed mechanism and provides a sensitive measurement of the FSS ($\delta/\hbar = 795.52 \pm 0.35$MHz for the quantum dot the setup described in this thesis was designed for) [2].

While it does not destroy entanglement, FSS is nonetheless undesirable for many applications. Many protocols require the ability to prepare a particular known entangled state,

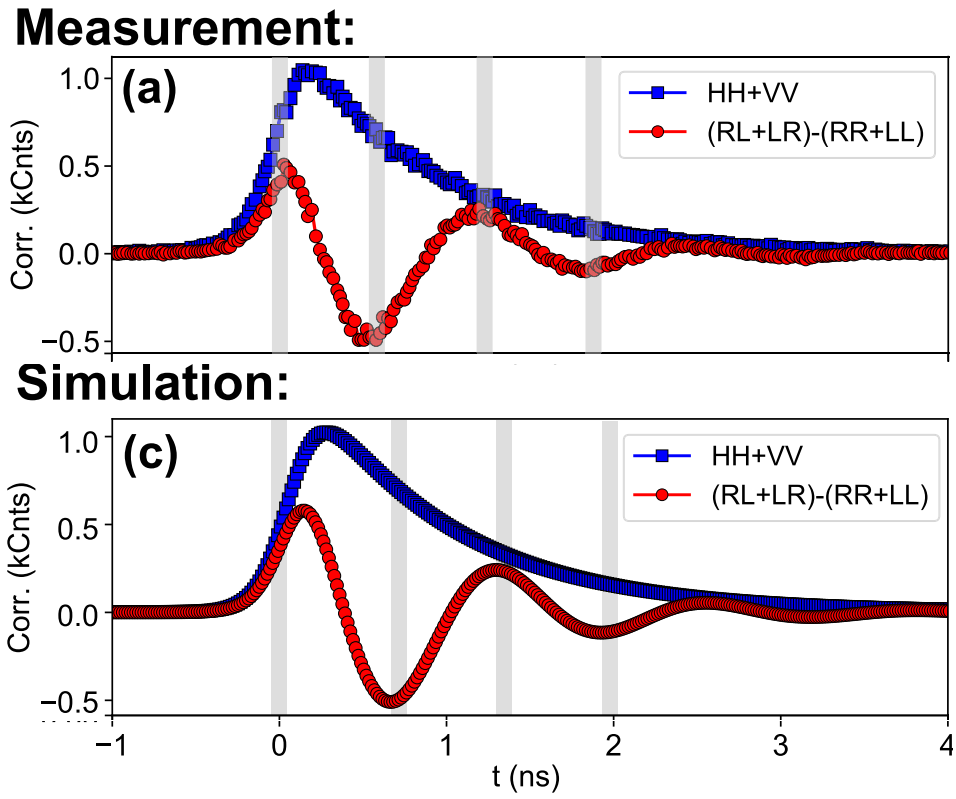

Figure 3.2: Quantum oscillations due to FSS in a quantum dot. The top figure shows the actual measurement result, and the bottom a simulation of expected measurement. Reprinted (adapted) with permission from [2]. Copyright 2019 American Chemical Society.

and this is only achievable with a precessing state by post-selecting photons within a narrow window of the exciton lifetime. Even when post-selecting, the rapid state precession degrades the measured quality of entanglement, as detectors have finite response times and will therefore necessarily integrate the evolving state over a time window of nonzero width, giving a measured ensemble that is not coherent. For these reasons, it is desirable to correct or "erase" the FSS.

3.3 Universal fine-structure splitting eraser scheme

Most approaches to date have focused on eliminating or compensating for the conditions leading to FSS within the quantum dot itself. These have included selecting growth methods which produce more symmetric dots and post-selecting dots with small FSS [52, 53], accelerating the exciton decay rate to reduce the effect of FSS [37], or using electric, magnetic or strain fields to reduce contributions from the electon-hole overlap β or the exciton wavefunction eccentricity ξ to Equation 3.1 [50]. These approaches are technically challenging, as they involve fabricating structures around existing sources.

The method presented in this thesis (published in [1]) is novel as it acts on the polarization state of the photons once they have been emitted without discarding a large percentage of the entangled photons. This approach is device-independent, and can be applied to any quantum dot with a FSS of up to tens of GHz (10GHz $\approx 40\mu$eV). The additional optical elements increase the overall device footprint, which may make it less desirable than other approaches in applications where compactness or portability are important factors.

3.3.1 HWP frequency shifting

When circularly polarized light is passed through a HWP rotating at frequency ω, the output will have its frequency shifted by 2ω. Garetz and Arnold [54] describe the behaviour using Jones calculus and provide a physical explanation in terms of conservation of angular momentum (similar to how light reflecting off of a moving mirror is Doppler shifted due to conservation of linear momentum). Mueller calculus cannot be used for this derivation, as it does not take into account the time varying nature of the electric fields.

A linear retarder is a device which affects the polarization of light by shifting the relative phase of two perpendicular components of the electric field without affecting the light's overall intensity. The Jones matrix for a linear retarder with retardance ϕ and fast axis θ is

$$\mathbf{LR}(\phi,\theta) = \begin{pmatrix} \cos(\phi/2) + i\sin(\phi/2)\cos(2\theta) & i\sin(\phi/2)\sin(2\theta) \\ i\sin(\phi/2)\sin(2\theta) & \cos(\phi/2) - i\sin(\phi/2)\cos(2\theta) \end{pmatrix} \tag{3.8}$$

Consider right circularly polarized light passing through a rotating HWP (discarding the global phase)

$$\begin{aligned}
\mathbf{LR}(\pi,\omega t)\mathrm{R} &= \begin{pmatrix} \cos(2\omega t) & \sin(2\omega t) \\ \sin(2\omega t) & -\cos(2\omega t) \end{pmatrix} \frac{1}{\sqrt{2}} \begin{pmatrix} 1 \\ i \end{pmatrix} \\
&= \frac{1}{\sqrt{2}} \begin{pmatrix} \cos(2\omega t) + i\sin(2\omega t) \\ \sin(2\omega t) - i\cos(2\omega t) \end{pmatrix} \\
&= \frac{1}{\sqrt{2}} \begin{pmatrix} \cos(2\omega t) + i\sin(2\omega t) \\ -i(\cos(2\omega t) + i\sin(2\omega t)) \end{pmatrix} \\
&= \frac{1}{\sqrt{2}} \begin{pmatrix} 1 \\ -i \end{pmatrix} \exp(2i\omega t) \\
&= \mathrm{L}e^{2i\omega t}
\end{aligned}$$

Writing the electric field of the output beam, we can see that for an input of right circularly polarized light with frequency ω_0, the output is left circularly polarized light with frequency $\omega_0 + 2\omega$

$$\vec{E} = \Re\left(e^{i\omega_0 t}\mathrm{L}e^{2i\omega t}\right) = \Re\left(e^{i(\omega_0+2\omega)t}\mathrm{L}\right) \tag{3.9}$$

Similarly, if circularly polarized light is passed through a HWP rotating in the direction opposite to the direction of polarization, the light will have its polarization direction reversed and its frequency shifted down by twice the waveplate's rate of rotation.

3.3.2 Optical fine-structure splitting eraser scheme

A fast rotating HWP's frequency shifting can be used to correct the fine-structure energy splitting (see Figure 3.3). The photons are first separated into biexciton (blue) and exciton (orange) paths using a diffraction grating (recall that the exciton an biexciton photons have different wavelengths due to the biexciton binding energy). The two paths are then sent through quarter-waveplate (QWP)s at $\pm 45^o$ to rotate the linearly polarized states such that

the higher energy $|H\rangle_{XX}$ and $|V\rangle_X$ become left circularly polarized and the lower energy $|V\rangle_{XX}$ and $|H\rangle_X$ become right circularly polarized. When passed through a rotating HWP, the higher energy left circularly polarized (LCP) will be shifted to a lower energy and the lower energy right circularly polarized (RCP) will be shifted to a higher energy. The end result is no energy splitting.

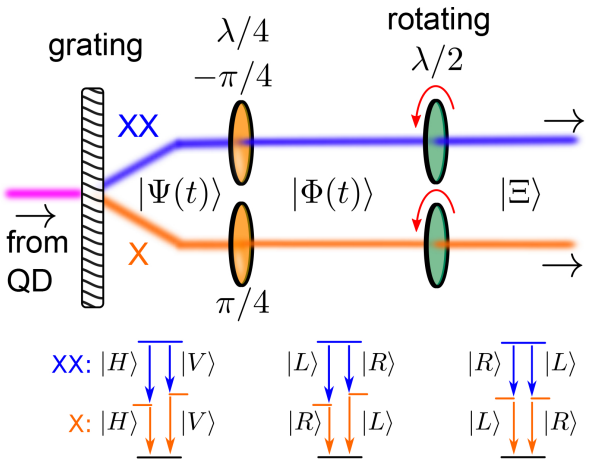

Figure 3.3: FSS eraser scheme. Prepared by A. Fognini and published in [1].

The HWP rotation frequency needs to shift the LCP frequency down by $\delta/2\hbar$ and the RCP frequency up by $\delta/2\hbar$ to get them to be at the same energy. Recall that a HWP rotating at frequency ω shifts circularly polarized light by 2ω, meaning the needed rotation frequency is $\omega_{HWP} = \delta/4\hbar$ or $f_{HWP} = \delta/8\pi\hbar$.

Chapter 4

Electro-optic fast half-waveplate

This chapter discusses the principles of how an electro-optic device can be used to rotate the polarization of light in a manner similar to a waveplate.

4.1 Polarization modulators

The rotation matrix (which is the lower 3×3 portion of a Mueller matrix) for a linear retarder is [55]

$$\mathbf{LR}(\phi,\theta) = \begin{pmatrix} \cos^2(2\theta) + \cos(\phi)\sin^2(2\theta) & (1-\cos(\phi))\cos(2\theta)\sin(2\theta) & -\sin(\phi)\sin(2\theta) \\ (1-\cos(\phi))\cos(2\theta)\sin(2\theta) & \cos(\phi)\cos^2(2\theta) + \sin^2(2\theta) & \sin(\phi)\cos(2\theta) \\ \sin(\phi)\sin(2\theta) & -\sin(\phi)\cos(2\theta) & \cos(\phi) \end{pmatrix} \quad (4.1)$$

where ϕ is the retardance (or phase shift) and θ is the angle of the retarder's fast axis. Variable polarization retarders, or modulators, typically have either a fixed retardance with a variable axis, or a fixed axis with a variable retardance. The two different scenarios are illustrated in Figure 4.1.

Variable axis modulators are typically realized by mounting a waveplate in a manual or motorized rotation stage. The rate of rotation is slow, at less than 1000 revolutions per

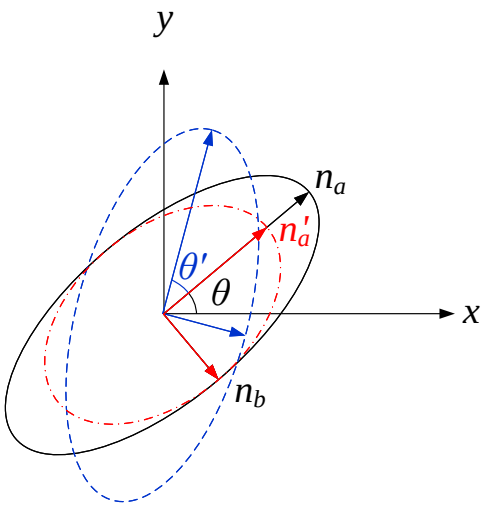

Figure 4.1: Index ellipse illustrating the difference between linear retarders with a fixed retardance and a variable axis (blue dashed), versus a fixed axis and a variable retardance (red dash-dot). The retardance ϕ in Equation 4.1 is a function of the difference in index of refraction between the fast (n_a) and slow (n_b) axes (see Equation 4.3).

.

second [55]. They can also be realized using ferro-electric liquid crystal cells, which have switching speeds on the order of 10μs [56].

Variable retardance modulators can be realized using liquid crystal cells (switching speeds of 5-100ms), electro-optic crystals (speeds of tens of GHz), photo-elastic effects (speeds of tens of kHz), or magneto-optic effects (which produces circular, rather than linear, retardance) [55].

None of these options provide us with both the type (rotating axis, fixed retardance) and speed (500MHz) of modulation we require. The next section introduces a variable axis retarder implemented using an electro-optic crystal which performs the type of modulation we need at the speed needed.

4.2 Electro-optic variable axis modulators

One solution is to use an atypical elecro-optic modulator geometry to vary the retardance of an electro-optic crystal along multiple axes in a way that imitates the behaviour of a fixed retardance, variable axis retarder, as first proposed by Buhrer *et al.* in 1962 [57].

4.2.1 The linear electro-optic effect

Crystal optics

Amorphous dielectric materials such as glasses which have random distribution of molecules tend to have macroscopic optical properties which do not depend on direction, and are said to be *isotropic* [58]. Even if the molecules forming the glass have properties that depend on direction (i.e. are *ANisotropic*), at macroscopic scales the effects of these tend to average out due to the random distribution. Crystals, by definition, do not have randomly distributed molecules. If the unit cells making up the crystal are not perfectly isotropic, then the macroscopic properties of the crystal will display anisotropy.

Optically anisotropic materials display different indices of refraction for light polarized along one or more of their axes. We represent the optical properties of anisotropic crystals using an impermeability tensor $\boldsymbol{\eta}$, which can be visualized using its corresponding index ellipsoid (Figure 4.2). The retardance ϕ encountered by polarized light propagating along axis $\vec{k}$ through a material of length L, $\phi = (n_a - n_b)L/\lambda$ is found by taking the lengths of the major (n_a) and minor (n_b) axes of the ellipse in the plane perpendicular to the direction of propagation.

The most general form of an ellipsoid centred at the origin is given by the quadric equation $1 = \eta_{11}x_1^2 + \eta_{22}x_2^2 + \eta_{33}x_3^2 + \eta_{12}x_1x_2 + \eta_{13}x_1x_3 + \eta_{23}x_2x_3 = \sum_{ij}\eta_{ij}x_ix_j$. This can be represented by a matrix (with some redundancy due to permutation symmetry $\eta_{ij} = \eta_{ji}$):

$$\boldsymbol{\eta} = \begin{bmatrix} \eta_{11} & \eta_{12} & \eta_{13} \\ \eta_{12} & \eta_{22} & \eta_{23} \\ \eta_{13} & \eta_{23} & \eta_{33} \end{bmatrix}$$

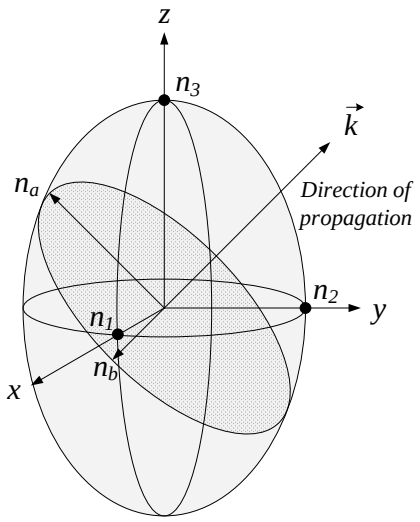

Figure 4.2: The index ellipsoid used for visualizing a material's optical anisotropy.

In the absence of any forces acting on the crystal, the off-axis terms will all be zero and the principal indices are the intercepts of the ellipsoid with the principal axes. In matrix form, they are the solutions to:

$$\begin{bmatrix} \frac{1}{n_1^2} & 0 & 0 \\ 0 & \frac{1}{n_2^2} & 0 \\ 0 & 0 & \frac{1}{n_3^2} \end{bmatrix} = \begin{bmatrix} \eta_{11} & 0 & 0 \\ 0 & \eta_{22} & 0 \\ 0 & 0 & \eta_{33} \end{bmatrix}$$

Electrically-induced anisotropy

Anything which distorts the positions, orientations or shapes of the unit cells or atoms of a crystal can lead to changes in the refractive indices of the crystal [59]. Dispersion is the most commonly observed phenomenon of this nature. Above a certain frequency, light passing through a crystal will interact resonantly with its electrons and in doing so change

the refractive index of the material. At much higher frequencies, the light will resonantly interact with the crystal lattice. These interactions lead to a frequency-dependent index of refraction, which causes wavelength-dependent pulse widening or contraction of signals which is an well-studied effect that is important in fibre optic communications. This effect is linear, meaning that the frequency dependence is the same for all intensities of light.

Certain crystals also display significant responses to low-frequency electric fields. The two most significant effects are the linear electro-optic (Pockels effect), which is proportional to the applied field, and quadratic electro-optic (Kerr effect), which is proportional to the square of the applied field. For this project, we are exclusively interested in the Pockels effect. Due to constraints on crystal symmetry and electric field symmetry to observe the effect, only crystals lacking an inversion centre display the Pockels effect, and the ways in which the field deforms the index ellipsoid depend primarily on crystal symmetry.

The effect of electric fields on the crystal along each of the principal axes is described by three matrices, one for each orthogonal component of the applied electric field. Due to the aforementioned redundancies, they are often written in a contracted form where the six possible coefficients of each matrix form the columns of a 6-by-3 matrix.

$$\begin{bmatrix} \mathfrak{r}_{\mathbf{1},k=1} & \mathfrak{r}_{\mathbf{1},k=2} & \mathfrak{r}_{\mathbf{1},k=3} \\ \mathfrak{r}_{\mathbf{2},k=1} & \mathfrak{r}_{\mathbf{2},k=2} & \mathfrak{r}_{\mathbf{2},k=3} \\ \mathfrak{r}_{\mathbf{3},k=1} & \mathfrak{r}_{\mathbf{3},k=2} & \mathfrak{r}_{\mathbf{3},k=3} \\ \mathfrak{r}_{\mathbf{4},k=1} & \mathfrak{r}_{\mathbf{4},k=2} & \mathfrak{r}_{\mathbf{4},k=3} \\ \mathfrak{r}_{\mathbf{5},k=1} & \mathfrak{r}_{\mathbf{5},k=2} & \mathfrak{r}_{\mathbf{5},k=3} \\ \mathfrak{r}_{\mathbf{6},k=1} & \mathfrak{r}_{\mathbf{6},k=2} & \mathfrak{r}_{\mathbf{6},k=3} \end{bmatrix} \Leftrightarrow \left\{ \begin{bmatrix} \mathfrak{r}_{\mathbf{1},k=1} & \mathfrak{r}_{\mathbf{6},k=1} & \mathfrak{r}_{\mathbf{5},k=1} \\ \mathfrak{r}_{\mathbf{6},k=1} & \mathfrak{r}_{\mathbf{2},k=1} & \mathfrak{r}_{\mathbf{4},k=1} \\ \mathfrak{r}_{\mathbf{5},k=1} & \mathfrak{r}_{\mathbf{4},k=1} & \mathfrak{r}_{\mathbf{3},k=1} \end{bmatrix} \begin{bmatrix} \mathfrak{r}_{\mathbf{1},k=2} & \mathfrak{r}_{\mathbf{6},k=2} & \mathfrak{r}_{\mathbf{5},k=2} \\ \mathfrak{r}_{\mathbf{6},k=2} & \mathfrak{r}_{\mathbf{2},k=2} & \mathfrak{r}_{\mathbf{4},k=2} \\ \mathfrak{r}_{\mathbf{5},k=2} & \mathfrak{r}_{\mathbf{4},k=2} & \mathfrak{r}_{\mathbf{3},k=2} \end{bmatrix} \begin{bmatrix} \mathfrak{r}_{\mathbf{1},k=3} & \mathfrak{r}_{\mathbf{6},k=3} & \mathfrak{r}_{\mathbf{5},k=3} \\ \mathfrak{r}_{\mathbf{6},k=3} & \mathfrak{r}_{\mathbf{2},k=3} & \mathfrak{r}_{\mathbf{4},k=3} \\ \mathfrak{r}_{\mathbf{5},k=3} & \mathfrak{r}_{\mathbf{4},k=3} & \mathfrak{r}_{\mathbf{3},k=3} \end{bmatrix} \right. \tag{4.2}$$

The new index ellipsoid is found by adding the changes to the original ellipsoid:

$$\eta_{ij}(\vec{E}) = \eta_{ij}(\vec{0}) + \sum_k \mathfrak{r}_{ijk} E_k$$

In general, the principal axes of the new ellipsoid may be rotated from their original position. As the off-axis terms vanish when the coordinate system is aligned with the ellipsoid's principal axes, the position of the new principal axes can be found by diagonalizing the matrix $\boldsymbol{\eta}$ to $\mathbf{D}$. The matrix $\mathbf{V}$ which satisfies $\mathbf{D} = \mathbf{V}^{-1}\boldsymbol{\eta}\mathbf{V}$ consists of $\boldsymbol{\eta}$'s eigenvalues along the columns, meaning that the eigenvectors point to the direction of the new axes. The lengths of the ellipsoid's principal axes are the diagonal elements of $\mathbf{D}$, which are also the eigenvalues of $\boldsymbol{\eta}$ [58].

We can describe the effect on the polarization of monochromatic light with wavelength λ propagating through an slab of non-chiral anisotropic material with index ellipsoid $\boldsymbol{\eta}$ of thickness t along direction $\vec{k}$ using the Mueller matrix for a linear retarder (Equation 4.1). There is a one to one relationship between the angle θ and the direction of the fast axis found by diagonalizing the matrix. The retardance ϕ is found from the lengths of the principal axes in the plane perpendicular to the direction of propagation (n_a and n_b in Figure 4.2):

$$\phi = \frac{t(n_a - n_b)}{\lambda} \tag{4.3}$$

4.2.2 Lithium niobate

Buhrer *et al.*'s proposal works with any electro-optic crystal with a 3-fold rotation axis, including symmetry groups cubic 23 and 43m, hexagonal 6' and 6m2, and trigonal 3, 32 and 3m [57]. Lithium niobate ($LiNbO_3$) is an ideal material for our implementation, as it has a compatible crystal symmetry (trigonal 3m), a high electro-optic response (meaning lower voltages can be used), excellent transparency in the IR range, high Currie temperature (which makes fabrication and handling easier and ensures good thermal stability) and good signal quality. High quality $LiNbO_3$ wafers are readily available at relatively low prices as the majority of early research work in integrated optics focused on $LiNbO_3$, and it continues to be widely used as a substrate material in commercial integrated optics devices [60]. Campbell *et al.* [61] were the first to successfully implement Buhrer *et al.*'s scheme using $LiNbO_3$ in 1971.

Lithium niobate has a crystal structure consisting of stacks of alternating lithium, niobium, and vacancies surrounded by oxygen octahedra. The stacks are used for defining the crystal's mirror planes and axis locations. It is a trigonal (meaning that it is symmetric for $2\pi/3$ rotations) 3m (meaning it has three vertical mirror planes) crystal. In the absence of an electric field, lithium niobate is a positive uniaxial crystal, meaning that the index ellipsoid is an oblate spheroid with the index of refraction being uniform in the xy plane ($n_1 = n_2 = n_o = 2.25$ at $\lambda = 840$nm and $T = 25^oC$ [62]), and having a smaller index of refraction in the z direction ($n_3 = n_e = 2.17$), which is its fast axis.

Note that the standard x-axis lies in one of the crystal's mirror planes, while the y-axis does not. The result of this is that even though the index ellipsoid forms a circle in the xy plane when $\vec{E} = \vec{0}$, the crystal responds differently to fields applied along the x and y axes. The Pockels coefficients for trigonal 3m crystals are shown below. In lithium niobate, the values of the coefficients at high modulation frequencies (RF or greater) and wavelengths close to 633 nm are $\mathfrak{r}_{51} = 18.2$ pm/V, $\mathfrak{r}_{22} = 3.4$ pm/V, $\mathfrak{r}_{13} = 7.7$ pm/V and $\mathfrak{r}_{33} = 28.8$ pm/V [62].

$$\mathfrak{r} = \begin{bmatrix} 0 & -\mathfrak{r}_{22} & \mathfrak{r}_{13} \\ 0 & \mathfrak{r}_{22} & \mathfrak{r}_{13} \\ 0 & 0 & \mathfrak{r}_{33} \\ 0 & \mathfrak{r}_{51} & 0 \\ \mathfrak{r}_{51} & 0 & 0 \\ -\mathfrak{r}_{22} & 0 & 0 \end{bmatrix} \tag{4.4}$$

4.2.3 Lithium niobate variable axis retarder

Rewriting $\mathfrak{r}$ in its less compact notation, we can express the index ellipsoid as a function of any electric field $\vec{E}$:

$$\bar{\eta}(\vec{E}) = \bar{\eta}(\vec{0}) + \sum_k \bar{\mathfrak{r}}_k E_k = \begin{bmatrix} \frac{1}{n_o^2} - \mathfrak{r}_{22}E_2 + \mathfrak{r}_{13}E_3 & -\mathfrak{r}_{22}E_1 & \mathfrak{r}_{51}E_1 \\ -\mathfrak{r}_{22}E_1 & \frac{1}{n_o^2} + \mathfrak{r}_{22}E_2 + \mathfrak{r}_{13}E_3 & \mathfrak{r}_{51}E_2 \\ \mathfrak{r}_{51}E_1 & \mathfrak{r}_{51}E_2 & \frac{1}{n_e^2} + \mathfrak{r}_{33}E_3 \end{bmatrix} \tag{4.5}$$

Now that we have the general form, we can constrain $\boldsymbol{\eta}$ to follow Burher *et al.*'s scheme. This involves three simplifications:

1. We propagate along the z-axis. This allows us to only consider the intersection of the ellipsoid with the xy plane.
2. There is no field in the direction of propagation (i.e. $E_3 = 0$).
3. There are electric fields in the x and y axes which are modulated in quadrature. We can express them as $E_1 = E_o \sin(\omega t),\ E_2 = E_o \cos(\omega t)$

Applying these simplifications yields:

$$\bar{\eta} = \begin{bmatrix} \frac{1}{n_o^2} - \mathfrak{r}_{22} E_o \cos(\omega_d t) & -\mathfrak{r}_{22} E_o \sin(\omega_d t) \\ -\mathfrak{r}_{22} E_o \sin(\omega_d t) & \frac{1}{n_o^2} + \mathfrak{r}_{22} E_o \cos(\omega_d t) \end{bmatrix} \tag{4.6}$$

Diagonalizing the matrix:

$$\begin{aligned} D &= V^{-1} \bar{\eta} V \\ &= \begin{bmatrix} -\frac{1}{\sqrt{2}} \sin(t\omega_d) & \cos^2(t\omega_d/2) \\ \frac{1}{2} \sin(t\omega_d) & \sin^2(t\omega_d/2) \end{bmatrix} \bar{\eta} \begin{bmatrix} -\cot(t\omega_d/2) & \tan(t\omega_d/2) \\ 1 & 1 \end{bmatrix} \\ &= \begin{bmatrix} \frac{1}{n_o^2} + E_o \mathfrak{r}_{22} & 0 \\ 0 & \frac{1}{n_o^2} - E_o \mathfrak{r}_{22} \end{bmatrix} \end{aligned} \tag{4.7}$$

We can find the direction of the major and minor axes from the columns of V:

$$\theta_a = \arctan\left(-\tan\left(\frac{t\omega_d}{2}\right)\right) = -\frac{t\omega_d}{2} \tag{4.8}$$

$$\theta_b = \arctan\left(\cot\left(\frac{t\omega_d}{2}\right)\right) = -\frac{t\omega_d}{2} \pm \frac{\pi}{2} \tag{4.9}$$

The indices of refraction along the major and minor axes in the rotated frame of reference are found by solving:

$$\frac{1}{n_b^2} = \frac{1}{n_o^2} + E_o \mathfrak{r}_{22} \implies n_b = n_o (1 + E_o \mathfrak{r}_{22} n_o^2)^{-1/2} \approx n_o - \frac{1}{2} E_o \mathfrak{r}_{22} n_o^3 \tag{4.10}$$

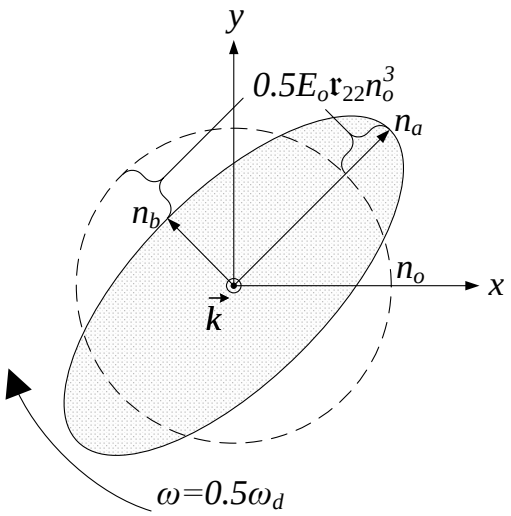

Figure 4.3: The index ellipse for the fast HWP described in Equation 4.6.

Similarly,

$$n_a \approx n_o + \frac{1}{2} E_o \mathfrak{r}_{22} n_o^3 \tag{4.11}$$

We are now able to write an approximate expression for the effective birefringence of our simulated HWP:

$$\Delta n = n_a - n_b \approx E_o \mathfrak{r}_{22} n_o^3 \tag{4.12}$$

In conclusion, by propagating along the z direction and applying fields in quadrature along the x and y directions with strengths E_o and frequency ω_d we get a variable-axis retarder rotating with frequency $\omega_d/2$ and having a birefringence of $E_o \mathfrak{r}_{22} n_o^3$.

4.3 Integrated optics

4.3.1 Why use a waveguide?

Campbell *et al.*'s device was capable of shifting 632.8nm light at a maximum rate of 110 MHz, well below the speed we need, while requiring a hefty 15W of input power [61]. This is because they were using bulk optics, meaning that the device did not act as a waveguide. This requires that the electrode separation be much larger than the beam diameter, which causes problems as a larger electrode separation requires a larger applied voltage to achieve the same electric field. Campbell *et al.*'s device, with an electrode separation of 1mm, had a half-wave voltage of 194 V. The challenges of producing high-voltage high-frequencies signals are further exacerbated by the fact that a crystal with two parallel plates acts as a capacitor, meaning that at high frequencies the power required increases substantially (Campbell *et al.* estimated an extra 1.6 W/MHz for their device).

The half-wave voltage (or voltage required to achieve a π phase shift) of a device can be found by combining equations 4.12 and 4.3 (setting $\phi = \pi$) with $E = V/d$, where d is the electrode separation and V is the applied voltage,

$$V_\pi = \frac{d\lambda\pi}{t\mathfrak{r}_{22}n_o^3} \tag{4.13}$$

where λ is the optical wavelength, and t is the device length. The half-wave voltage can be reduced in two ways: by reducing the electrode separation or by increasing the length of the device. Increasing the length beyond a few centimetres is undesirable, both because longer devices have greater optical loss (the absorption coefficient of bulk $LiNbO_3$ is about $\alpha = 0.3cm^{-1}$ in the near-infrared region, or about a 30% loss in intensity over 10cm [63]) and greater electrical losses.

The separation of the electrodes can be greatly reduced by coupling the light into a waveguide, thereby both reducing the beam's diameter and fixing its location in the device. For this reason, as well as for integration with optical fibres or other integrated optics, modern EOMs feature a waveguide. The increase in speed and reduction in power are

quite remarkable. For example, Qin *et al.* demonstrated a $LiNbO_3$ variable-axis modulator capable of shifting 780nm light at a rate of 2 GHz, with a half-wave voltage of about 20V and a driving power of 1W [64]. This is an order of magnitude reduction in both voltage and power from what was required by Campbell *et al.*, while also having an order of magnitude increase in operating frequency.

4.3.2 Waveguide fabrication methods

There exist a number of methods for fabricating waveguides in lithium niobate [65, 66]. The most common by far are titanium diffusion and proton exchange; however, the device supplied to us makes use of zinc oxide diffusion.

In proton exchange, lithium niobate is exposed to a liquid source of hydrogen (such as benzoic acid) at a high temperature, causing Li^+ ions to be replaced by H^+ ions which increases n_e and decreases n_o. This technique does not work for variable-axis retarders, as waveguides made this way behave similar to polarization maintaining fibres and can only guide light polarized parallel to the z-axis.

Waveguides formed by titanium diffusion are able to support multiple polarization modes, but are highly susceptible to photorefractive damage at wavelengths below 1550nm. Photorefractive damage refers to optically induced changes in the index of refraction which are the result of charge migration. Electrons from impurities are excited to the conduction band and migrate until they fall into traps. Over time, this can lead to the formation of a net electric field, which changes the refractive index through the electro-optic effect . While these effects occur in all lithium niobate, titanium diffusion significantly lowers the damage threshold by increasing the number of electron donors (damage thresholds are as low as tens of nW for single mode waveguides at 633nm [67]). While this is not a problem for the quantum dot signal, as a practical matter it is necessary to be able to use beams of a few microwatts at least to align the experiment and perform preliminary characterization measurements to determine appropriate input signals.

The device supplied for this experiment used zinc oxide diffusion, first proposed and demonstrated by Young *et al.* [68]. These waveguides are able to support polarizations aligned along both axes and have much higher photorefractive damage thresholds than titanium diffusion (Young *et al.* reported it to be 4 orders of magnitude higher).

4.3.3 Electrode Geometry

Our device has electrodes patterned onto the top (see figure 4.4). Instead of generating x and y fields by applying a voltage across perpendicular sets of electrodes, the field components are generated by applying common and differential voltages to the outer electrodes.

We still apply sinusoidal signals to two channels, but they have different characteristics than in the perpendicular pairs of electrodes case. There are four independent signal parameters that allow for control of the field:

1. Amplitude of the sinusoidal signals (both will require the same amplitude due to symmetry): Controls the overall strength of the field applied
2. Relative phase shift: controls the relative strength of the field in the x and y directions by varying the portion of the signal which is common vs differential (The signal is 100% common when the two signals are perfectly in phase, 100% differential when they are perfectly out of phase, and 50% common and 50% differential when they are applied in quadrature). This also controls the rotation direction of the waveplate.
3. Common DC offset (corrects one component of waveguide birefringence)
4. Differential DC offset (corrects other component of waveguide birefringence)

While it is possible to correct the waveguide birefringence with either a common or differential DC offset alone, in the general case a much lower voltage is required if a linear combination of the two is used.

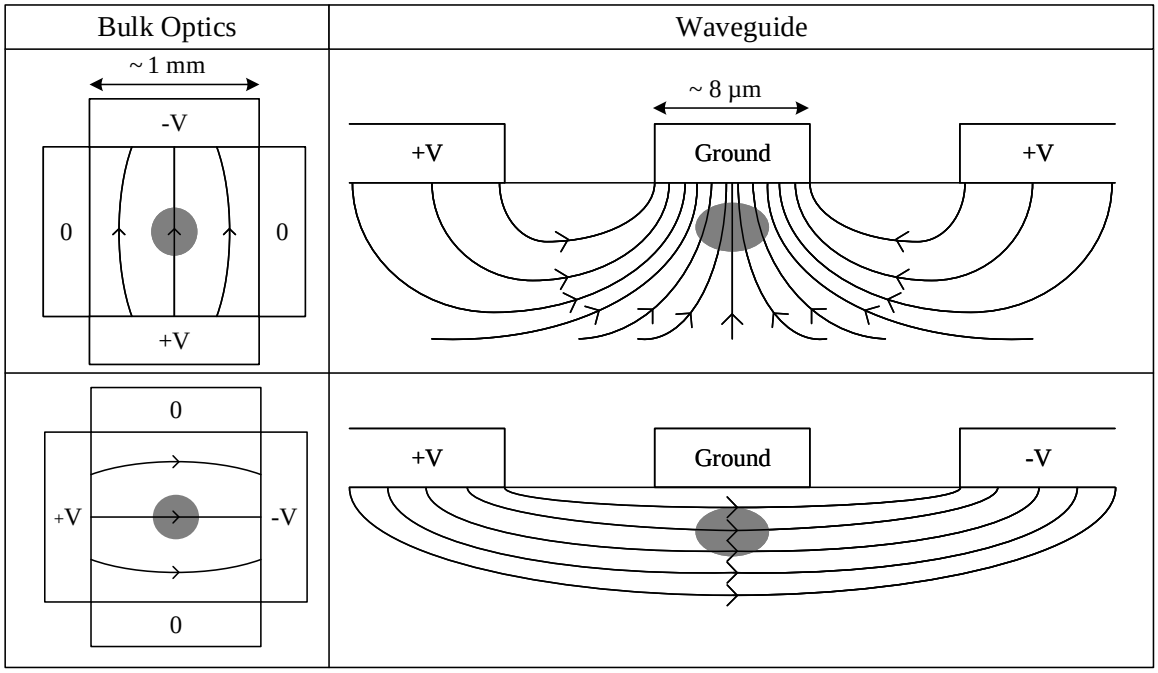

Figure 4.4: Digram comparing how x and y fields are produced by applying common (top right panel) and differential (bottom right panel) voltages to the surface electrodes in a waveguide EOM to the electrode geometry used in a bulk optical device such as those proposed by Burher *et al.* [57] and Campbell *et al.* [61] (left panels).

4.4 Device particulars

The device used for this experiment was purchased from SRICO[1]. The devices are similar to those supplied by SRICO to [64], except with different waveguide dimensions to support operation at 890nm. The devices have a 3cm electrode length along a ZnO diffused waveguide in the 3.2-4.4cm-long x-cut $LiNbO_3$ wafers. The wafer is housed in a package with SMA connectors to which the electrodes are connected. A fabrication method similar to that described in [69] was used by the supplier.

[1]Website: https://www.srico.com/

Chapter 5

Device characterization

5.1 Optical coupling

Before the behaviour of the EOM can be studied, good optical coupling to the device's waveguide needs to be achieved and verified.

5.1.1 Mounting

The device was mounted using a 5-axis stage with an F=30mm lens in a 1-axis (along the beam axis) linear stage mounted to the same platform to collimate the output beam. The light was coupled in using an Olympus LMPlan5xIR objective (NA: 0.1) on a 4-axis stage. Both stages were mounted to a small breadboard to facilitate movement of the set up. See Figure 5.1.

The light can be coupled into the waveguide by looking at the output mode on using a pellicle and CCD camera or on an IR card. The output beam path is aligned using 4 of the 5-axis stage's degrees of freedom (x position, y position, tip, tilt), and the coupling is achieved using the 4-axis stage's degrees of freedom (x position, y position, tip, tilt) and one of the 5-axis stage's degrees of freedom (z position).

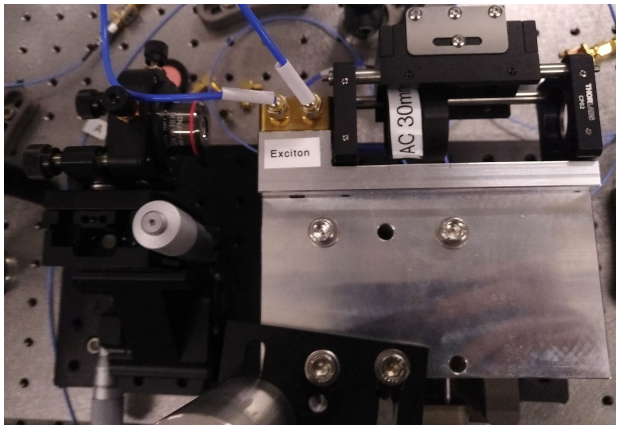

Figure 5.1: Top-view photo of opto-mechanical set up for coupling light in and out of EOM. Light passes from the left to the right of the image.

5.1.2 Mode profile

The output mode of the EOM waveguide is shown in Figure 5.2. The mode has a similar width in both directions, and is approximately Gaussian in the plane parallel to the device surface. The mode in the plane perpendicular to the device's surface shows some asymmetry, likely due to the waveguide being adjacent to the device's surface.

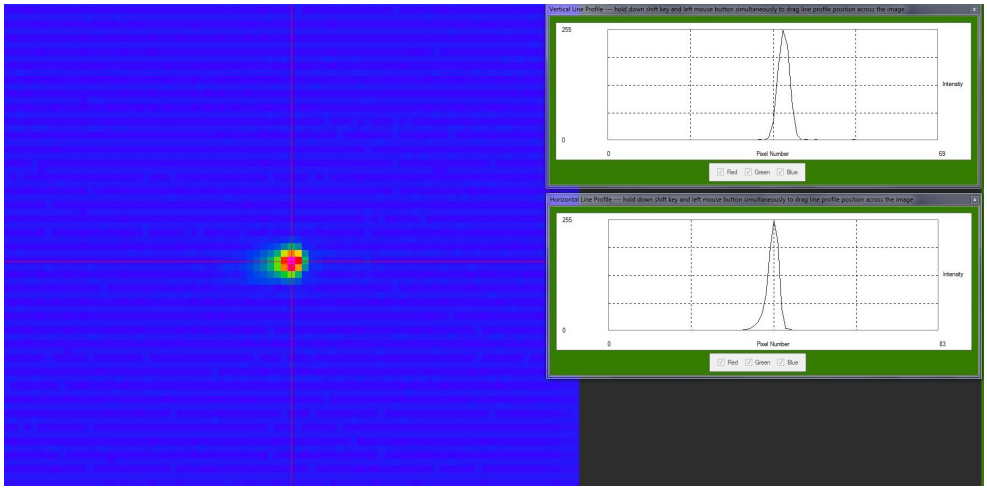

Figure 5.2: EOM waveguide mode profile imaged on a CCD camera. Plots show cross-sections along lines shown in false-colour image.

Note that the laser spot size was too large for the waveguide, resulting in some of the light passing though the crystal outside of the waveguide. We had an excess of intensity available and only light which passed through the waveguide remained collimated after passing through the collimating lens, so for simplicity we used an iris placed some distance after from the collimating lens rather than using a telescope to change the beam size.

5.2 DC polarization tomography measurements

Characterization with low-frequency signals is a lower-complexity first step to measure the device's responsiveness to applied voltages and estimate how much RF power will be required. We used measurements in 18 polarization bases with a slowly varying applied voltage to characterize the voltage dependence of the device birefringence.

5.2.1 Principles

In order to completely describe the effect of a lossless optical element on polarization, we need to find the values of the nine components of its rotation matrix, which is the lower right 3x3 portion of its Mueller matrix

$$M = \begin{pmatrix} 1 & 0 & 0 & 0 \\ 0 & m_{11} & m_{12} & m_{13} \\ 0 & m_{21} & m_{22} & m_{23} \\ 0 & m_{31} & m_{32} & m_{33} \end{pmatrix} \tag{5.1}$$

State preparation

We start by preparing an input polarization of H, D, or R. We first polarize the input light to H using a polarizing beamsplitter (PBS)

$$\begin{pmatrix} 0.5 & 0.5 & 0 & 0 \\ 0.5 & 0.5 & 0 & 0 \\ 0 & 0 & 0 & 0 \\ 0 & 0 & 0 & 0 \end{pmatrix} \begin{pmatrix} s_{i0} \\ s_{i1} \\ s_{i2} \\ s_{i3} \end{pmatrix} = \begin{pmatrix} 0.5s_{i0} + 0.5s_{01} \\ 0.5s_{i0} + 0.5s_{i1} \\ 0 \\ 0 \end{pmatrix} \triangleq I_0 \begin{pmatrix} 1 \\ 1 \\ 0 \\ 0 \end{pmatrix} \tag{5.2}$$

We then select an appropriate waveplate to rotate the state to the desired input polarization. No rotation is required for the case of H, so we simply remove the input waveplate entirely.

We use a HWP ($LR(\phi = \pi, \theta = 22.5^o)$) to get diagonally polarized light

$$\begin{pmatrix} 1 & 0 & 0 & 0 \\ 0 & 0 & 1 & 0 \\ 0 & 1 & 0 & 0 \\ 0 & 0 & 0 & 1 \end{pmatrix} \begin{pmatrix} I_0 \\ I_0 \\ 0 \\ 0 \end{pmatrix} = I_0 \begin{pmatrix} 1 \\ 0 \\ 1 \\ 0 \end{pmatrix} \tag{5.3}$$

We use a QWP ($LR(\phi = \pi/2, \theta = 45^o)$) to get right circularly polarized light

$$\begin{pmatrix} 1 & 0 & 0 & 0 \\ 0 & 0 & 0 & -1 \\ 0 & 0 & 1 & 0 \\ 0 & 1 & 0 & 0 \end{pmatrix} \begin{pmatrix} I_0 \\ I_0 \\ 0 \\ 0 \end{pmatrix} = I_0 \begin{pmatrix} 1 \\ 0 \\ 0 \\ 1 \end{pmatrix} \tag{5.4}$$

In this way we can prepare H, D and RCP polarized light with intensity I_0. Using $k = 1$ to denote the no waveplate case, $k = 2$ to denote the HWP case and $k = 3$ to denote the QWP case we can represent our input state as

$$\begin{pmatrix} I_0 \\ I_0\delta_{1,k} \\ I_0\delta_{2,k} \\ I_0\delta_{3,k} \end{pmatrix} \tag{5.5}$$

where $\delta_{n,k}$ is the Kronecker delta function.

State interaction

Once we have prepared the input state, we can pass the beam through the device under investigation.

$$\begin{pmatrix} 1 & 0 & 0 & 0 \\ 0 & m_{11} & m_{12} & m_{13} \\ 0 & m_{21} & m_{22} & m_{23} \\ 0 & m_{31} & m_{32} & m_{33} \end{pmatrix} \begin{pmatrix} I_0 \\ I_0\delta_{1,k} \\ I_0\delta_{2,k} \\ I_0\delta_{3,k} \end{pmatrix} = I_0 \begin{pmatrix} 1 \\ m_{1k} \\ m_{2k} \\ m_{2k} \end{pmatrix} \tag{5.6}$$

We now have a polarization state whose Stokes parameters correspond to one of the columns of the Mueller matrix of the device under study.

State measurement

We will use a non-polarizing beamsplitter (NPBS) with transmission factor $T = 1 - R$ to provide information on the total intensity of the beam (S_0). After the NPBS, the polarization is unchanged but the total intensity is $I' = I_0 - I_{BS} = \frac{R}{T} I_{BS}$

We then use a second waveplate and HWP to get information about each of the other three Stokes parameters (S_1,S_2,S_3).

We use no waveplate to get information on S_1

$$\begin{pmatrix} 0.5 & 0.5 & 0 & 0 \\ 0.5 & 0.5 & 0 & 0 \\ 0 & 0 & 0 & 0 \\ 0 & 0 & 0 & 0 \end{pmatrix} \begin{pmatrix} \frac{R}{T} I_{BS} \\ \frac{R}{T} I_{BS} m_{1k} \\ \frac{R}{T} I_{BS} m_{2k} \\ \frac{R}{T} I_{BS} m_{2k} \end{pmatrix} = 0.5 \frac{R}{T} I_{BS} \begin{pmatrix} 1 + m_{1k} \\ 1 + m_{1k} \\ 0 \\ 0 \end{pmatrix} \tag{5.7}$$

We use a HWP ($\phi = \pi, \theta = 22.5^o$) to get information on S_2

$$\begin{pmatrix} 0.5 & 0.5 & 0 & 0 \\ 0.5 & 0.5 & 0 & 0 \\ 0 & 0 & 0 & 0 \\ 0 & 0 & 0 & 0 \end{pmatrix} \begin{pmatrix} 1 & 0 & 0 & 0 \\ 0 & 0 & 1 & 0 \\ 0 & 1 & 0 & 0 \\ 0 & 0 & 0 & 1 \end{pmatrix} \begin{pmatrix} \frac{R}{T} I_{BS} \\ \frac{R}{T} I_{BS} m_{1k} \\ \frac{R}{T} I_{BS} m_{2k} \\ \frac{R}{T} I_{BS} m_{2k} \end{pmatrix} = 0.5 \frac{R}{T} I_{BS} \begin{pmatrix} 1 + m_{2k} \\ 1 + m_{2k} \\ 0 \\ 0 \end{pmatrix} \tag{5.8}$$

We use a HWP ($\phi = \pi/2, \theta = 45^o$) to get information on S_3

$$\begin{pmatrix} 0.5 & 0.5 & 0 & 0 \\ 0.5 & 0.5 & 0 & 0 \\ 0 & 0 & 0 & 0 \\ 0 & 0 & 0 & 0 \end{pmatrix} \begin{pmatrix} 1 & 0 & 0 & 0 \\ 0 & 0 & 0 & -1 \\ 0 & 0 & 1 & 0 \\ 0 & 1 & 0 & 0 \end{pmatrix} \begin{pmatrix} \frac{R}{T} I_{BS} \\ \frac{R}{T} I_{BS} m_{1k} \\ \frac{R}{T} I_{BS} m_{2k} \\ \frac{R}{T} I_{BS} m_{2k} \end{pmatrix} = 0.5 \frac{R}{T} I_{BS} \begin{pmatrix} 1 - m_{3k} \\ 1 - m_{3k} \\ 0 \\ 0 \end{pmatrix} \tag{5.9}$$

Our S_0 values, which are what are measured on the photodiodes, give us the relationship

$$I_{PBS} = \frac{R}{2T} I_{BS}(1 + (1 - 2\delta_{3,j}) m_{jk}) \tag{5.10}$$

We now have measurements which allow us to figure out all nine values of the rotation matrix. We determine which column we are probing by choosing our input waveplate, and which row we are measuring by choosing our output waveplate.

5.2.2 Set up

We used the experimental set up shown in Figure 5.3 to measure the voltage-dependent polarization modulation of the EOM.

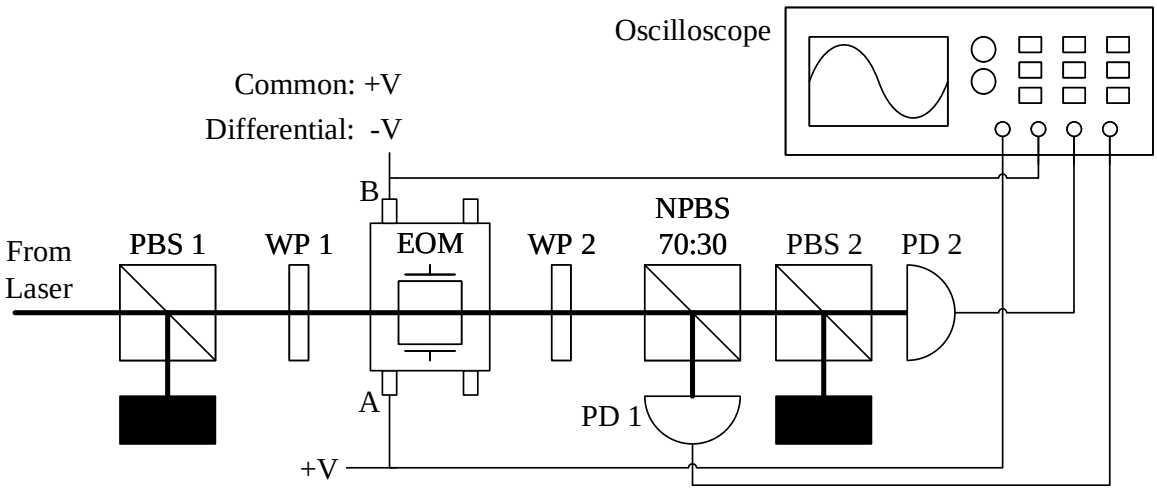

Figure 5.3: Experimental set up for measuring the EOM Mueller matrix as a function of electrode voltage.

We input a triangular waveform with a peak to peak voltage of 10V, and recorded two sets, one with the common input voltage configuration and one with the differential voltage configuration, of the 9 output waveforms for different permutations of WP 1 and WP 2 described in subsection 5.2.1. Each of the 18 measurements included four waveforms: the voltage applied to EOM port A, the voltage applied to EOM port B, the signal from the

photodiode on the reflection port of the NPBS, and the signal from photodiode after the HWP.

We assume that the two photodiode signals are related to the optical intensity by some linear factor: $V_{BS} = \alpha_{BS} I_{BS}$ and $V_{PBS} = \alpha_{PBS} I_{PBS}$. Then becomes $V_{PBS} = \frac{\alpha_{PBS}}{\alpha_{BS}} \frac{R}{2T} V_{BS}(f(m_{jk}))$. If we define $C = \frac{\alpha_{PBS}}{\alpha_{BS}} \frac{R}{2T}$, which should be a constant independent of time or applied voltage and $V = V_{PBS}/V_{BS}$, we now have

$$V_{jk} = C(1 + (1 - 2\phi_{3,j})m_{jk}) \tag{5.11}$$

where we use no waveplate, a HWP at 22.2^o and a HWP at 45^o for WP 1 to get $j = 1, 2, 3$ respectively, and no waveplate, a HWP at 22.2^o and a HWP at 45^o for WP 2 to get $k = 1, 2, 3$.

5.2.3 Results

The curves are shown in Figure 5.4. There is an inadequate amount of the response measured (less than a full period for all of the curves) to get a good fit to the data; however, there are three main conclusions which can be drawn from a qualitative inspection:

1. There is a substantial portion, but less than the entirety, of a full period visible. This suggests that the half-wave voltage (V_π) is larger than 10V but likely less than 20V.

2. The V_{RL} local minima are non-zero in both the common and differential case. This suggests that the waveguide birefringence is not aligned with the direction of the fields generated by either differential or common voltages.

These results were used to inform the selection of electronic components. A DC source with two channels capable of supplying up to ±35V and amplifiers with a rail voltage of 24V were selected for trying to perform RF frequency shifting.

5.3 RF frequency shifting

The goal of demonstrating efficient RF frequency shifting is to:

1. Validate the ability of the device to operate as a good approximation of a rotating HWP.
2. Determine the appropriate signal parameters to achieve good operation. These values will be used in future experiments.

5.3.1 Principles

Errors in the phase, amplitude or DC offset of applied signals results in incomplete conversion of the carrier signal, conversion of the signal to the undesired sideband, and generation of higher harmonics. The effects of various errors in terms of x and y field is summarized in Table 5.1

In the case of an integrated optics EOM using the electrode geometry in Figure 4.4, the field-magnitude maladjustment is due to the amplitude of the signals (which are equal in both electrodes), the amplitude imbalance and phase imbalance maladjustments are both caused by improper phase between the two electrode signals, and the DC bias in drive field error is caused by waveguide birefringence and corrected by application of a DC bias (which will in general be a different value for each electrode).

5.3.2 Methods

Signal generation

The sinsoidal signals were generated using a Texas Instruments DAC38RF82EVM digital-to-analog converter (DAC) evaluation module. The device can be configured to generate

RELATIVE AMPLITUDES OF OUTPUT-BEAM COMPONENTS FOR VARIOUS MODULATOR MALADJUSTMENTS

Maladjustment	Applied Fields: X Component	Applied Fields: Y Component	Polarization[a]	Frequency: $\omega - 2\omega_m$	$\omega - \omega_m$	ω	$\omega + \omega_m$	$\omega + 2\omega_m$	$\omega + 3\omega_m$
None (ideal case)	$\sin \omega_m t$	$\cos \omega_m t$	C						
			S				1		
Field-magnitude error	$(1 - \delta) \sin \omega_m t$	$(1 - \delta) \cos \omega_m t$	C			$\pi\ \delta/2$			
			S				1		
Amplitude imbalance	$(1 + \delta) \sin \omega_m t$	$\cos \omega_m t$	C	$\pi\ \delta/8$		$\pi\ \delta/4$		$\pi\ \delta/8$	
			S		$\delta/4$		1		$\delta/4$
Phase imbalance	$\sin (\omega_m t + \delta)$	$\cos \omega_m t$	C	$\pi\ \delta/8$				$\pi\ \delta/8$	
			S		$\delta/4$		$1 + i\ \delta/2$		$\delta/4$
Second harmonic in drive field	$\sin \omega_m t + \delta \sin 2\ \omega_m t$	$\cos \omega_m t + \delta \cos 2\ \omega_m t$	C		$\pi\ \delta/4$		$\pi\ \delta/4$		X
			S	X	X	$\delta/2$	1	$\delta/2$	X
Dc bias in drive field	$\sin \omega_m t$	$\delta + \cos \omega_m t$	C		$\pi\ \delta/4$		$\pi\ \delta/4$		X
			S	X	X	$\delta/2$	1	$\delta/2$	X
Electrodes not parallel to crystal axis ($E_z = \sin \delta \cos \omega_m t$)	$\sin \omega_m t$	$\cos \delta \cos \omega_m t$	C	$\pi\ \delta^2/16$		$\pi\ \delta^2/8$		$\pi\ \delta^2/16$	
			S		$\delta^2/8$		1		$\delta^2/8$
Reverse-polarized component of relative amplitude δ in input beam	same as ideal case		C		δ				
			S				1		
Light beam at an angle δ relative to the crystal axis ($\delta \leq 1$ mrad)	same as ideal case		C	$\pi r\ \delta/4$				$\pi r\ \delta/4$	
			S		$r\ \delta$		$1; r\ \delta/2$		$r\ \delta/2$

[a] C—carrier polarization; S—desired sideband polarization.

Table 5.1: Contributions of modulating signal maladjustments to undesired output-beam components by frequency and polarization. Reprinted from [61] with permission of publisher. ©1971, IEEE.

sinusoidal signals using its on-chip oscillator. Code written by Andreas Fognini[1] can be used to control the frequency (0-4 GHz with a step size of 0.00003 Hz), phase (360 degree, with 0.005 degree steps), and amplitude (1023 steps). For this experiment, the frequency was set at 350 MHz.

I measured the relationship between the amplitude setting in the code and the output power. The results are shown in Table 5.2.

There is a slight difference in response between channels A and B; however, it is within 1% for all amplitudes and less than the expected discrepancies between channels introduced by other electrical components so the difference was ignored. Note that the signals are applied to both ports of each of the electrodes, rather than terminating one of the terminals.

[1]Code available at https://github.com/afognini/PyDualDDS

Input		0	0.1	0.2	0.3	0.4	0.5	0.6	0.7	0.8	0.9	1
Measured	Ch A	1.33	26.4	53.5	76.2	106	133	160	187	213	241	268
[mVrms]	Ch B	1.33	26.1	53.2	80.8	108	135	163	191	218	246	273

Table 5.2: Amplitude setting versus measured output amplitude for DAC. All measurements have an uncertainty of 500μV.

This reduced the power loss in the system, and was feasible due to the relatively low frequency of operation (hundreds of MHz rather than tens of GHz).

After the DAC and attenuator, the signal was sent to a MiniCircuits ZHL-20W-52-S high power amplifier. At 350MHz the amplifier has a gain of 50.5dB and an output power at the 1dB compression point of 43.8dBm according to the supplier, which means the input signal should be kept well below -6.7dBm to minimize distortion. The DAC can produce signals up to about 0.27Vrms (1.638dBm), so attenuation well over 8.5dB is needed to ensure safe operation with minimal distortion. We choose to start with a large attenuation and decrease it as needed while searching for the correct amplitude.

Set up

A schematic of the optical an electrical set up is shown in Figure 5.5. The laser is a Thorlabs DBR852P distributed bragg reflector diode laser with a centre wavelength of 852nm (352THz) and a linewidth of $\leq$ 10MHz. PBS and HWPs are used together as circular polarizers (+45 ^{o} passes right circularly polarized (R) light and -45 ^{o} passes left circularly polarized (L) light). The HWP was used to correct for the effects of a device birefringence which did not appear to be correlated with degradation in the quality of signal conversion.

The frequency of the output light was measured using a Thorlabs SA200-8B scanning Fabry-Perot interferometer, which has a 1.5 GHz free spectral range (FSR) and a finesse of at least 200 (250 typical). The cavity length was controlled using a function generator

applying a low-frequency (< 10Hz) triangle waveform whose offset and amplitude were adjusted as needed to centre the desired peaks within the scanning range.

Parameter sweeping

Each of the undesirable peaks in Table 5.1 can be contributed to by multiple maladjustments, and we observed that changing one parameter has an effect on the input setting to actual output relationship for the other parameters, probably due to changes in the impedance of the EOM. Both of these factors make it infeasible to independently optimize each parameter.

Due to the sensitivity of the measurement (each sample is 4 MHz apart, which corresponds to a shift in wavelength of only 0.01nm), the position of the peaks moves with time due to very slight fluctuations in temperature and current supplied by the laser's controller. This makes it impossible to label peaks based on absolute position alone. This, along with the equal spacing between all of the peaks and wide variation in heights down to undetectably levels makes it extremely challenging to label each of the peaks in a data set without referring to other data sets. This made extracting the optimal parameters from an automated parameter sweep infeasible.

Table 5.1 still provides useful information which can help with intuition when manually optimizing the parameters, particularly when using a circular polariser to look at the carrier and sideband (RCP and LCP respectively for an input polarization of RCP) separately. Setting amplitudes and running a continuous sweep of the relative phase while manually adjusting the DC offset proved to be a successful approach.

5.3.3 Results

Figure 5.6 shows the signal from the Fabry Perot interferometer's photodiode for the best achieved signal, with the peaks labelled.

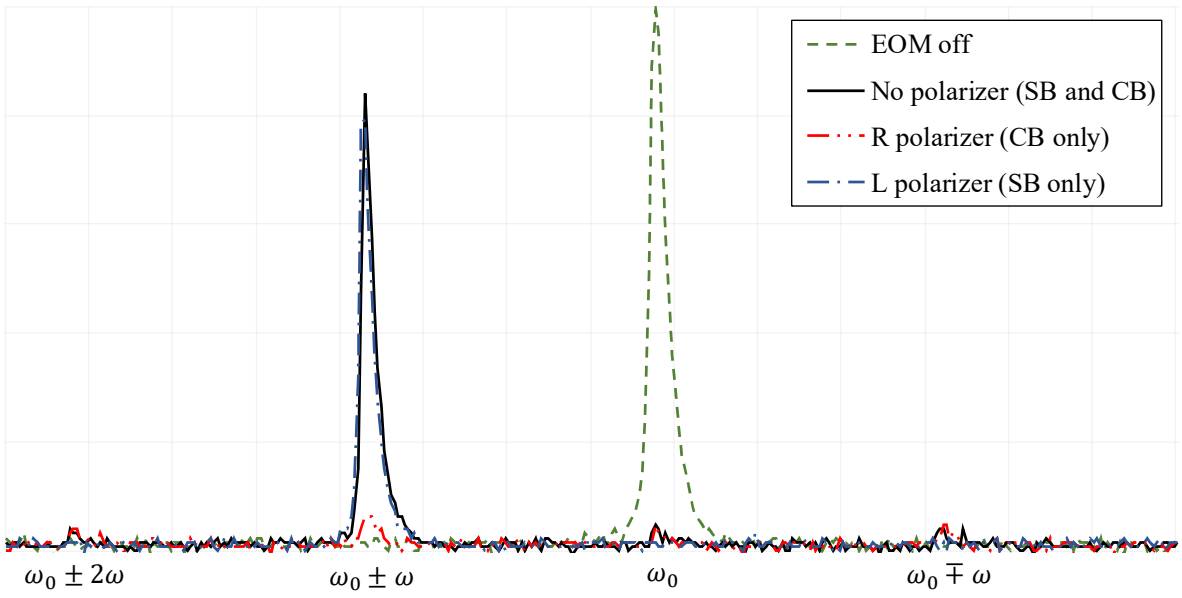

Figure 5.6: Signal from fabry-perot interferometer over a single bias voltage scan for four measurement configurations, showing frequency shifting. The first curve (green dashed line) shows the frequency content of the beam when no signal is applied to the EOM electrodes, with all of the power in the carrier band (ω_0). For the second curve (black solid line) the EOM is turned on and no polariser is used at the output (i.e. the PBS in front of the interferometer is removed). Note that almost all of the power is in one of the side bands ($\omega_0 \pm \omega$), though there is still some power in the carrier band, undesired side band ($\omega_0 \mp \omega$) and the second-harmonic for the desired side band ($\omega_0 \pm 2\omega$). For the third curve (red dot-dot-dash line) the QWP in front of the interferometer is set at $+45^o$ and the PBS is replaced, allowing only RCP light to pass. For the final curve (blue dot-dash line) the QWP in front of the interferometer is set at -45^o, allowing only LCP light to pass. Note that all of the undesired peaks are completely suppressed.

The peaks have separations of 87-88 sample points, and we expect them to be 350 MHz apart, meaning the samples are approximately 4 MHz apart. Using the cavity's FSR and typical finesse, we expect a resolution of approximately 7.5 MHz. A Lorentzian fit to the

carrier band peak with the EOM off yields a FWHM of 19 ± 2 MHz.

Using numerical integration to compute the approximate area under each curve after subtracting the background level, the percentage of power found in each peak when no polariser is used are: desired side band: 92.6%, carrier band: 3.3%, opposite side band: 2.5%, second-order side band: 1.6%.

The settings used for the curve in Figure 5.6 are:

DC A: -13.19 V

DC B: +15.73 V

Phase: 350^o

Amplitude: 0.95 - 14dB

The amplitude setting of 0.95 corresponds to an output of approximately 257mVrms or 1.209dBm. With an attenuation of -14dB the power after the amplifier is therefore approximately 37.7dBm, which corresponds to a peak voltage of about 24V for a 50ohm system. The impedance of the EOM is unknown and varies with applied signal, and though applying the signal to both ends of each electrode simultaneously should result in a similar voltage, if not power, being applied. It is also worth noting that the required DC bias drifts slightly over the course of several minutes due to charge migration [62]. The effect can be mitigated by adjusting the bias as needed, minimizing the length of time the device is operated continuously, and taking breaks to allow the charges to relax back by removing the bias or applying a bias of reverse polarity.

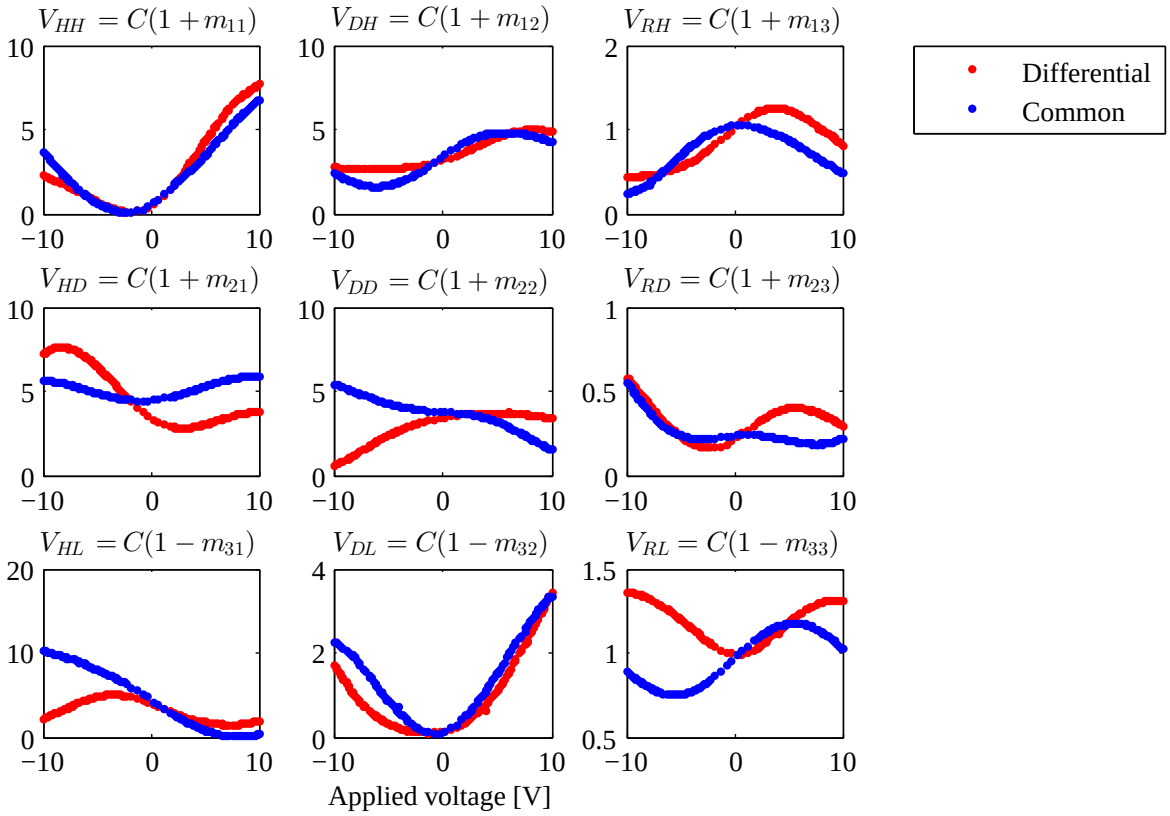

Figure 5.4: Low frequency polarization tomography of EOM electro-optic response for differential and common cases. The y-axis is $V_{jk} = V_{PBS}/V_{BS}$ computed from the output of the two photodiodes in Figure 5.4.

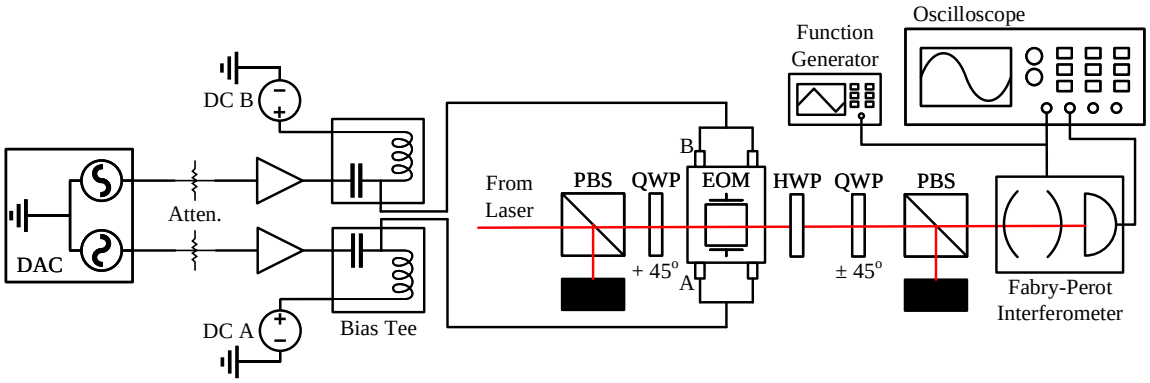

Figure 5.5: Schematic representation of the optical and electrical set up for performing and measuring frequency shifting.

Chapter 6

Summary and future steps

Quantum dots are a promising source of entangled photons which have the potential to overcome the limitations of SPDC sources making on-demand operation possible. Photonic nanostructures such as semiconductor nanowires increase collection efficiencies from quantum dots, and sources with little or no dephasing have already been demonstrated. A remaining challenge is the state precession caused by FSS, which can be compensated or erased using standard optical components and a fast rotating HWP.

An EOM made from x-cut lithium niobate can be used to emulate a HWP rotating at speeds up to tens of GHz, which makes erasing FSS of up to a few tens of μeV possible. I present data showing a conversion efficiency of 92% at a wavelength of 852nm and a modulation frequency of 350 MHz.

Future steps involve demonstrating frequency conversion with single photons, and eventually implementing the fine-structure eraser scheme on an entangled photon source.

References

[1] A. Fognini *et al.*, "Universal fine-structure eraser for quantum dots," *Opt. Express*, vol. 26, no. 19, pp. 24 487–24 496, Sep 2018. [Online]. Available: https://doi.org/10.1364/OE.26.024487

[2] A. Fognini *et al.*, "Dephasing free photon entanglement with a quantum dot," *ACS Photonics*, vol. 6, no. 7, pp. 1656–1663, 2019. [Online]. Available: https://doi.org/10.1021/acsphotonics.8b01496

[3] A. Einstein, B. Podolsky, and N. Rosen, "Can quantum-mechanical description of physical reality be considered complete?" *Phys. Rev.*, vol. 47, pp. 777–780, May 1935. [Online]. Available: https://doi.org/10.1103/PhysRev.47.777

[4] J. S. Bell, "On the einstein podolsky rosen paradox," *Physics Physique Fizika*, vol. 1, pp. 195–200, Nov 1964. [Online]. Available: https://doi.org/10.1103/PhysicsPhysiqueFizika.1.195

[5] J. F. Clauser *et al.*, "Proposed experiment to test local hidden-variable theories," *Phys. Rev. Lett.*, vol. 23, pp. 880–884, Oct 1969. [Online]. Available: https://doi.org/10.1103/PhysRevLett.23.880

[6] V. Giovannetti, S. Lloyd, and L. Maccone, "Quantum-enhanced measurements: Beating the standard quantum limit," *Science*, vol. 306, no. 5700, pp. 1330–1336, 2004. [Online]. Available: https://science.sciencemag.org/content/306/5700/1330

[7] M. Lanzagorta, "Quantum radar," *Synthesis Lectures on Quantum Computing*, vol. 3, no. 1, pp. 1–139, 2011. [Online]. Available: https://doi.org/10.2200/S00384ED1V01Y201110QMC005

[8] C. H. Bennett and S. J. Wiesner, "Communication via one- and two-particle operators on einstein-podolsky-rosen states," *Phys. Rev. Lett.*, vol. 69, pp. 2881–2884, Nov 1992. [Online]. Available: https://doi.org/10.1103/PhysRevLett.69.2881

[9] C. H. Bennett and G. Brassard., "Quantum cryptography: Public key distribution and coin tossing," p. 175–179.

[10] P. W. Shor, "Algorithms for quantum computation: discrete logarithms and factoring," in *Proceedings 35th Annual Symposium on Foundations of Computer Science*, Nov 1994, pp. 124–134.

[11] R. Feynman, "Simulating physics with computers," vol. 21, p. 467. [Online]. Available: https://doi.org/10.1007/BF02650179

[12] S. Lloyd, "Universal quantum simulators," *Science*, vol. 273, no. 5278, pp. 1073–1078, 1996. [Online]. Available: http://www.jstor.org/stable/2899535

[13] C.-Y. Lu and J.-W. Pan, "Push-button photon entanglement," *Nature Photonics*, vol. 8, pp. 174 EP –, Feb 2014. [Online]. Available: https://doi.org/10.1038/nphoton.2014.29

[14] A. Aspect, P. Grangier, and G. Roger, "Experimental tests of realistic local theories via bell's theorem," *Phys. Rev. Lett.*, vol. 47, pp. 460–463, Aug 1981. [Online]. Available: https://doi.org/10.1103/PhysRevLett.47.460

[15] A. Orieux *et al.*, "Semiconductor devices for entangled photon pair generation: a review," *Reports on Progress in Physics*, vol. 80, no. 7, p. 076001, May 2017. [Online]. Available: https://doi.org/10.1088%2F1361-6633%2Faa6955

[16] E. Knill, R. Laflamme, and G. J. Milburn, "A scheme for efficient quantum computation with linear optics," *nature*, vol. 409, no. 6816, p. 46, 2001.

[17] C. K. Hong, Z. Y. Ou, and L. Mandel, "Measurement of subpicosecond time intervals between two photons by interference," *Phys. Rev. Lett.*, vol. 59, pp. 2044–2046, Nov 1987. [Online]. Available: https://doi.org/10.1103/PhysRevLett.59.2044

[18] M. A. Nielsen and I. Chuang, *Quantum computation and quantum information*. Cambridge University Press, 2000.

[19] J. L. O'Brien *et al.*, "Demonstration of an all-optical quantum controlled-not gate," *Nature*, vol. 426, no. 6964, p. 264, 2003.

[20] E. Knill, "Bounds on the probability of success of postselected nonlinear sign shifts implemented with linear optics," *Phys. Rev. A*, vol. 68, p. 064303, Dec 2003. [Online]. Available: https://doi.org/10.1103/PhysRevA.68.064303

[21] P. G. Kwiat *et al.*, "New high-intensity source of polarization-entangled photon pairs," *Phys. Rev. Lett.*, vol. 75, pp. 4337–4341, Dec 1995. [Online]. Available: https://doi.org/10.1103/PhysRevLett.75.4337

[22] B. Hensen *et al.*, "Loophole-free bell inequality violation using electron spins separated by 1.3 kilometres," *Nature*, vol. 526, pp. 682 EP –, Oct 2015. [Online]. Available: https://doi.org/10.1038/nature15759

[23] L. K. Shalm *et al.*, "Strong loophole-free test of local realism," *Phys. Rev. Lett.*, vol. 115, p. 250402, Dec 2015. [Online]. Available: https://doi.org/10.1103/PhysRevLett.115.250402

[24] M. Giustina *et al.*, "Significant-loophole-free test of bell's theorem with entangled photons," *Phys. Rev. Lett.*, vol. 115, p. 250401, Dec 2015. [Online]. Available: https://doi.org/10.1103/PhysRevLett.115.250401

[25] J.-L. Smirr *et al.*, "Intrinsic limitations to the quality of pulsed spontaneous parametric downconversion sources for quantum information applications," *J. Opt. Soc. Am. B*, vol. 28, no. 4, pp. 832–841, Apr 2011. [Online]. Available: https://doi.org/10.1364/JOSAB.28.000832

[26] M. A. Broome *et al.*, "Reducing multi-photon rates in pulsed down-conversion by temporal multiplexing," *Opt. Express*, vol. 19, no. 23, pp. 22 698–22 708, Nov 2011. [Online]. Available: http://www.opticsexpress.org/abstract.cfm?URI=oe-19-23-22698

[27] Y.-P. Huang and P. Kumar, "Antibunched emission of photon pairs via quantum zeno blockade," *Phys. Rev. Lett.*, vol. 108, p. 030502, Jan 2012. [Online]. Available: https://doi.org/10.1103/PhysRevLett.108.030502

[28] M. Barbieri *et al.*, "Parametric downconversion and optical quantum gates: two's company, four's a crowd," *Journal of Modern Optics*, vol. 56, no. 2-3, pp. 209–214, 2009. [Online]. Available: https://doi.org/10.1080/09500340802337374

[29] M. Fox, *Quantum optics: an introduction*. Oxford University Press, 2006.

[30] K. Edamatsu, "Entangled photons: Generation, observation, and characterization," *Japanese Journal of Applied Physics*, vol. 46, no. 11, pp. 7175–7187, nov 2007. [Online]. Available: https://doi.org/10.1143%2Fjjap.46.7175

[31] O. Benson *et al.*, "Regulated and entangled photons from a single quantum dot," *Phys. Rev. Lett.*, vol. 84, pp. 2513–2516, Mar 2000. [Online]. Available: https://doi.org/10.1103/PhysRevLett.84.2513

[32] D. Huber *et al.*, "Semiconductor quantum dots as an ideal source of polarization-entangled photon pairs on-demand: a review," *Journal of Optics*, vol. 20, no. 7, p. 073002, Jun 2018. [Online]. Available: https://doi.org/10.1088%2F2040-8986%2Faac4c4

[33] W. Barnes *et al.*, "Solid-state single photon sources: light collection strategies," *The European Physical Journal D - Atomic, Molecular, Optical and Plasma Physics*, vol. 18, no. 2, pp. 197–210, Feb 2002. [Online]. Available: https://doi.org/10.1140/epjd/e20020024

[34] Y. Chen *et al.*, "Highly-efficient extraction of entangled photons from quantum dots using a broadband optical antenna," *Nature Communications*, vol. 9, no. 1, p. 2994, 2018. [Online]. Available: https://doi.org/10.1038/s41467-018-05456-2

[35] S. Liu *et al.*, "A deterministic quantum dot micropillar single photon source with >65% extraction efficiency based on fluorescence imaging method," *Scientific Reports*, vol. 7, no. 1, p. 13986, 2017. [Online]. Available: https://doi.org/10.1038/s41598-017-13433-w

[36] P. Senellart, G. Solomon, and A. White, "High-performance semiconductor quantum-dot single-photon sources," *Nature Nanotechnology*, vol. 12, p. 1026, Nov 2017, review Article. [Online]. Available: https://doi.org/10.1038/nnano.2017.218

[37] A. Dousse *et al.*, "Ultrabright source of entangled photon pairs," *Nature*, vol. 466, p. 217, Jul 2010. [Online]. Available: https://doi.org/10.1038/nature09148

[38] H. Wang *et al.*, "On-demand semiconductor source of entangled photons which simultaneously has high fidelity, efficiency, and indistinguishability," *Phys. Rev. Lett.*, vol. 122, p. 113602, Mar 2019. [Online]. Available: https://doi.org/10.1103/PhysRevLett.122.113602

[39] T. H. Chung *et al.*, "Selective carrier injection into patterned arrays of pyramidal quantum dots for entangled photon light-emitting diodes," *Nature Photonics*, vol. 10, p. 782, Oct 2016. [Online]. Available: https://doi.org/10.1038/nphoton.2016.203

[40] R. Hafenbrak *et al.*, "Triggered polarization-entangled photon pairs from a single quantum dot up to 30 k," *New Journal of Physics*, vol. 9, no. 9, pp. 315–315, 2007. [Online]. Available: https://doi.org/10.1088/1367-2630/9/9/315

[41] Scarani, V. *et al.*, "Four-photon correction in two-photon bell experiments," *Eur. Phys. J. D*, vol. 32, no. 1, pp. 129–138, 2005. [Online]. Available: https://doi.org/10.1140/epjd/e2004-00170-7

[42] X.-L. Wang *et al.*, "Experimental ten-photon entanglement," *Phys. Rev. Lett.*, vol. 117, p. 210502, Nov 2016. [Online]. Available: https://doi.org/10.1103/PhysRevLett.117.210502

[43] K. D. Jöns *et al.*, "Bright nanoscale source of deterministic entangled photon pairs violating bell's inequality," *Scientific Reports*, vol. 7, no. 1, p. 1700, 2017. [Online]. Available: https://doi.org/10.1038/s41598-017-01509-6

[44] D. Dalacu *et al.*, "Ultraclean emission from InAsP quantum dots in defect-free wurtzite InP nanowires," *Nano Letters*, vol. 12, no. 11, pp. 5919–5923, Nov 2012. [Online]. Available: https://doi.org/10.1021/nl303327h

[45] M. A. M. Versteegh *et al.*, "Observation of strongly entangled photon pairs from a nanowire quantum dot," *Nature Communications*, vol. 5, p. 5298, Oct 2014. [Online]. Available: https://doi.org/10.1038/ncomms6298

[46] P. E. Faria Junior *et al.*, "Realistic multiband $k \cdot p$ approach from ab initio and spin-orbit coupling effects of InAs and InP in wurtzite phase," *Phys. Rev. B*, vol. 93, p. 235204, Jun 2016. [Online]. Available: https://doi.org/10.1103/PhysRevB.93.235204

[47] U. Perinetti, "Optical properties of semiconductor quantum dots." [Online]. Available: http://resolver.tudelft.nl/uuid:d67a6277-9fbe-4df6-bfd2-8f54c24e9572

[48] "Examples in quantum mechanics: Finite round square well bound states," course notes, College of Saint Benedict and Saint John's University. [Online]. Available: http://www.physics.csbsju.edu/QM/square.09.html

[49] M. Mastrovich, "Characterizing single photon emission from quantum dots in nanowires," 2019. [Online]. Available: http://hdl.handle.net/10012/14727

[50] M. Zeeshan *et al.*, "Proposed scheme to generate bright entangled photon pairs by application of a quadrupole field to a single quantum dot," *Phys. Rev. Lett.*, vol. 122, p. 227401, Jun 2019. [Online]. Available: https://doi.org/10.1103/PhysRevLett.122.227401

[51] M. Bayer *et al.*, "Fine structure of neutral and charged excitons in self-assembled In(Ga)As/(Al)GaAs quantum dots," *Phys. Rev. B*, vol. 65, p. 195315, May 2002. [Online]. Available: https://doi.org/10.1103/PhysRevB.65.195315

[52] Y. H. Huo, A. Rastelli, and O. G. Schmidt, "Ultra-small excitonic fine structure splitting in highly symmetric quantum dots on GaAs (001) substrate," *Applied Physics Letters*, vol. 102, no. 15, p. 152105, 2013. [Online]. Available: https://doi.org/10.1063/1.4802088

[53] M. H. M. van Weert *et al.*, "Selective excitation and detection of spin states in a single nanowire quantum dot," *Nano Letters*, vol. 9, no. 5, pp. 1989–1993, 2009, pMID: 19341258. [Online]. Available: https://doi.org/10.1021/nl900250g

[54] B. A. Garetz and S. Arnold, "Variable frequency shifting of circularly polarized laser radiation via a rotating half-wave retardation plate," *Optics Communications*, vol. 31, no. 1, pp. 1 – 3, 1979. [Online]. Available: https://doi.org/10.1016/0030-4018(79)90230-X

[55] *Handbook of optics*, 3rd ed. New York: McGraw-Hill, 2010, vol. 1.

[56] H.-R. Kim *et al.*, "A rotatable waveplate using a vertically aligned deformed-helix ferroelectric liquid crystal," *Ferroelectrics*, vol. 312, no. 1, pp. 57–62, 2004. [Online]. Available: https://doi.org/10.1080/00150190490511536

[57] C. F. Buhrer, D. Baird, and E. M. Conwell, "Optical frequency shifting by electro-optic effect," *Applied Physics Letters*, vol. 1, no. 2, pp. 46–49, 1962. [Online]. Available: https://doi.org/10.1063/1.1753701

[58] B. E. A. Saleh, *Fundamentals of photonics*, ser. Wiley series in pure and applied optics. New York ; Toronto: Wiley, 1991.

[59] I. P. Kaminow, *An introduction to electrooptic devices*. New York: Academic Press, 1974.

[60] M. Bass *et al.*, *Handbook of Optics, Third Edition Volume I: Geometrical and Physical Optics, Polarized Light, Components and Instruments*, 3rd ed. New York, NY, USA: McGraw-Hill, Inc., 2010.

[61] J. Campbell and W. Steier, "Rotating-waveplate optical-frequency shifting in lithium niobate," *IEEE Journal of Quantum Electronics*, vol. 7, no. 9, pp. 450–457, 1971. [Online]. Available: https://doi.org/10.1109/JQE.1971.1076830

[62] R. S. Weis and T. K. Gaylord, "Lithium niobate: Summary of physical properties and crystal structure," *Applied Physics A*, vol. 37, no. 4, pp. 191–203, Aug 1985. [Online]. Available: https://doi.org/10.1007/BF00614817

[63] Z. Jiangou *et al.*, "Optical absorption properties of doped lithium niobate crystals," *Journal of Physics: Condensed Matter*, vol. 4, no. 11, p. 2977, 1992. [Online]. Available: https://doi.org/10.1088/0953-8984/4/11/022

[64] C. Qin *et al.*, "Single-tone optical frequency shifting and nonmagnetic optical isolation by electro-optical emulation of a rotating half-wave plate in a traveling-wave lithium niobate waveguide," *IEEE Photonics Journal*, vol. 9, no. 3, pp. 1–13, June 2017. [Online]. Available: https://doi.org/10.1109/JPHOT.2017.2695458

[65] M. Bazzan and C. Sada, "Optical waveguides in lithium niobate: Recent developments and applications," *Applied Physics Reviews*, vol. 2, no. 4, p. 040603, 2015. [Online]. Available: https://doi.org/10.1063/1.4931601

[66] J. E. Toney, *Lithium Niobate Photonics*. Artech House, 2015.

[67] R. V. Schmidt, P. S. Cross, and A. M. Glass, "Optically induced crosstalk in LiNbO3 waveguide switches," *Journal of Applied Physics*, vol. 51, no. 1, pp. 90–93, 1980. [Online]. Available: https://doi.org/10.1063/1.327307

[68] W. M. Young *et al.*, "Photorefractive-damage-resistant Zn-diffused waveguides in MgO:LiNbO3," *Opt. Lett.*, vol. 16, no. 13, pp. 995–997, Jul 1991. [Online]. Available: https://doi.org/10.1364/OL.16.000995

[69] J. E. Toney *et al.*, "ZnO-diffused lithium niobate waveguide polarization controller," in *Integrated Optics: Devices, Materials, and Technologies XX*, vol. 9750. International Society for Optics and Photonics, 2016, p. 975008. [Online]. Available: https://doi.org/10.1117/12.2210999